

# Dark-Sector Deformations of Holographic Anisotropic Superfluids in Asymptotically Hyperscaling Violation Geometry

Ji-Seong Chae<sup>†1</sup>

<sup>†</sup>*Department of Physics, Hanyang University, Seoul 04763, Korea*

## Abstract

We study dark-sector deformations of holographic anisotropic  $p$ -wave superfluids in hyperscaling-violating black-brane backgrounds. In the visible  $SU(2)$  sector,  $b(u)$  fixes the chemical potential and charge density, while  $\omega(u)$  condenses and selects a boundary direction, producing anisotropic strip entanglement. The visible critical chemical potential, radial profiles, condensate branch, and strip-entanglement difference vary with dimension and hyperscaling-violating exponents. We then add hidden gauge sectors and hidden dark-scalar portals. Hidden-current mixing gives a solvable example, whereas isotropic dark sources cancel in the strip difference. For the kinetic dark-scalar portal,  $Z_{\text{dm}}(\Phi)$  deforms the Yang–Mills operator; hence  $b_0(u)$ ,  $\omega_1(u)$ , and the order- $\epsilon^2$  anisotropic stress are computed in the same deformed problem. The critical shift depends on the hyperscaling-violating background and can change sign. The main result is a strip susceptibility at vanishing portal strength. It is negative in the  $D = 4$  and  $D = 5$  backgrounds, so the portal weakly suppresses visible strip anisotropy. This has a holographic RG interpretation: the normalizable dark scalar is weighted toward the IR horizon, while narrow strips probe the UV near-boundary RT region. Thus, the portal decouples in the UV and the susceptibility vanishes quadratically with strip width; wider strips reach deeper into the bulk and recover the IR dark-sector effects.

arXiv:2606.24328v2 [hep-th] 24 Jun 2026

---

<sup>1</sup>jiseongchae17@gmail.com

# Contents

<b>1</b>	<b>Introduction</b>	<b>3</b>
<b>2</b>	<b>Model and equations of motion</b>	<b>5</b>
2.1	Visible sector: Anisotropic holographic superfluid . . . . .	6
2.2	Visible SU(2) Yang–Mills sector . . . . .	7
2.2.1	Thermodynamic meaning of the reference transition . . . . .	9
2.3	General dark-sector deformations of the Yang–Mills equations . . . . .	10
2.3.1	Case I: temporal hidden U(1) gauge sector . . . . .	11
2.3.2	Case II: hidden SU(2) with kinetic mixing . . . . .	12
2.3.3	Case III-a: hidden dark scalar with a mass portal . . . . .	14
2.3.4	Case III-b: hidden dark scalar with a kinetic portal (tensor portal) . . . . .	15
<b>3</b>	<b>Visible HSV scaling and dark-sector response</b>	<b>15</b>
3.1	Visible critical point before dark-sector deformation . . . . .	16
3.2	General dark-sector deformation of the critical operator . . . . .	17
3.3	Minimal hidden SU(2) as a solvable benchmark . . . . .	18
3.4	How the exact rescaling is lost . . . . .	18
<b>4</b>	<b>RT surfaces, HEE response, and the condensate</b>	<b>19</b>
4.1	RT observables: interval, strip, slab, and orientation anisotropy . . . . .	19
4.2	Dark-sector source rules and null channels . . . . .	20
4.3	Tensor-portal susceptibility as a linear response coefficient . . . . .	21
4.4	Nonlinear condensate and extraction of $\langle O \rangle$ . . . . .	22
<b>5</b>	<b>Dark-sector response</b>	<b>23</b>
5.1	Selection rule and rigid benchmark . . . . .	23
5.2	Tensor-portal susceptibility and short-distance decoupling . . . . .	24
5.3	Critical scale and HSV-dependent sign change . . . . .	25
5.4	Self-consistent radial profiles and cancellation mechanism . . . . .	27
5.5	Condensate branches below the critical point . . . . .	28
<b>6</b>	<b>Discussion</b>	<b>29</b>
6.1	Boundary interpretation of the dark deformations . . . . .	29
6.2	What HSV adds beyond the asymptotically AdS superfluid . . . . .	30
6.3	Physical reading of the result in different dimensions . . . . .	31
6.4	Limitations and future works . . . . .	31
<b>A</b>	<b>Supplementary figures and consistency checks</b>	<b>33</b>
A.1	Additional Case-II $\alpha_{\text{dm}}$ overlays . . . . .	33
A.2	Supporting figures in $D = 3$ . . . . .	37
A.3	Supporting figures in $D = 4$ . . . . .	38

A.4 Supporting figures in  $D = 5$  . . . . . 39

# 1 Introduction

Gauge/gravity duality turns certain strongly coupled quantum systems into classical gravitational boundary-value problems. The original correspondence relates large- $N$  conformal gauge theories to gravity on asymptotically AdS spaces [1, 2, 3, 4]. Its real-time prescription identifies infalling bulk perturbations with retarded correlators of boundary operators [5, 6]. This is the reason why black-brane perturbations can compute transport coefficients and order-parameter responses in regimes where a quasiparticle description is unavailable.

A major lesson of the holographic transport program is that universal behavior is often tied to symmetry and channel structure. In isotropic Einstein gravity, transverse gravitons behave as minimally coupled massless fields, leading to the familiar shear-viscosity result  $\eta/s = 1/4\pi$  [7, 8, 9]. The membrane-paradigm derivation explains this universality as a horizon-coupling statement rather than a microscopic accident [6]. Fluid/gravity constructions then gave a systematic derivative-expansion interpretation of the same black-brane data [10, 11].

Anisotropic holographic superfluids are important precisely because they break this simple channel equivalence. In the non-Abelian  $p$ -wave construction, a temporal  $SU(2)$  component sources a chemical potential while a spatial component condenses and selects a boundary direction [12, 13]. The condensate is dual to a vector current expectation value, schematically  $\langle J_{x_1}^1 \rangle$ , so the ordered phase breaks both the visible  $SU(2)$  flavor symmetry and spatial rotational symmetry. In such a phase, perturbations parallel and transverse to the ordered direction need not probe the same effective coupling. This mechanism underlies the non-universal shear response of anisotropic holographic superfluids [14, 15, 16]. It also motivates using anisotropic observables, rather than only scalar thermodynamic quantities, to detect hidden-sector imprints.

The dark-sector motivation comes from kinetic mixing and portal interactions. Hidden gauge sectors are generic in many extensions of the Standard Model, and Abelian kinetic mixing gives a simple low-energy portal between visible and hidden currents [17, 18, 19, 20, 21]. Holographic superconductors with dark matter sectors showed that such mixing can shift critical data, magnetic response, vortices, condensate flow and entanglement entropy [22, 23, 24, 25, 26, 27, 28, 29, 30]. In phase-sensitive devices, such as holographic SQUIDs, a small hidden-sector coupling can become visible because the measured quantity is a difference or interference signal rather than a large absolute condensate amplitude [31]. In two-current Dirac-fluid models, the same idea appears as a hidden charge channel in the transport matrix [32, 33].

In the present work, we investigate the dark-sector deformation of the anisotropic superfluid in the hyperscaling-violation geometry. In that setting, the hidden sector is not merely an extra charge reservoir: once the  $p$ -wave condensate breaks rotations, the hidden sector couples differently to fluctuation channels aligned with and transverse to the order parameter [34]. This is why an anisotropic background is advantageous. A dark deformation that would look like a mild rescaling in an isotropic phase can become a directional source for holographic entanglement entropy ( $S_{\parallel}, S_{\perp}$ ), shear response, or the vector-order condensate.

The remaining question is why the analysis should be extended beyond asymptotically AdS back-

grounds. Asymptotic AdS corresponds to a relativistic UV fixed point, but many strongly correlated systems are better described over intermediate scales by non-relativistic scaling with a dynamical exponent  $z$  and an effective hyperscaling-violation exponent  $\vartheta$ . Hyperscaling-violating geometries arise naturally in Einstein-Maxwell-dilaton effective theories and provide candidate gravity descriptions of scale-covariant finite-temperature and finite-density systems [35, 36, 37, 38]. The HSV black brane is therefore an effective bulk dual for a boundary theory characterized by finite density, non-relativistic scaling and an effective spatial dimensionality shifted by  $\vartheta$ .

The field-theory dictionary in this effective HSV background is concrete enough for the purpose of this work. The Abelian field supporting charge density is dual to a conserved boundary current and its chemical potential. The visible SU(2) Yang-Mills field is dual to a global flavor current multiplet  $J_\mu^a$ . The temporal visible component sources the third flavor charge, while the spatial component  $B_{x_1}^1$  gives the vector condensate  $\langle J_{x_1}^1 \rangle$ . A hidden  $U(1)$  or hidden SU(2) gauge field is therefore interpreted as a hidden conserved current sector. A kinetic-mixing term in the bulk implements a current-current portal between visible and hidden sectors. A scalar or tensor portal implements a scale-dependent deformation of the visible current kinetic operator, or equivalently a deformation of the radial weights controlling the visible current correlator.

This interpretation also clarifies what is new in the HSV extension. The HSV exponents change the radial Sturm-Liouville weights of the vector zero mode, the electric profile, and the Ryu-Takayanagi kernels. Consequently, a dark-sector coupling that is a simple constant factor in AdS can become a profile-dependent deformation in HSV. Conversely, if a dark-sector response remains an exact factor across  $D = 3, 4, 5$  and across HSV parameters, that behavior is a nontrivial universality check. Recent work on anisotropic holographic superfluids in asymptotically HSV geometries provides the visible-sector analytic baseline we deform here [39]. More broadly, recent reconstruction and entanglement studies beyond asymptotic AdS emphasize that non-AdS scaling geometries can encode physically meaningful boundary response over finite radial or energy windows [40, 41, 42].

Entanglement entropy is a natural observable for this program because it is sensitive to geometry and orientation. The Ryu-Takayanagi prescription converts a boundary subregion into a bulk extremal area [43, 44]. Shape dependence, extrinsic geometry and first-law variations provide a controlled way to diagnose small metric deformations [45, 46, 47, 48, 49, 50, 51, 52]. In the anisotropic phase we therefore compare interval entropy in  $D = 3$  and strip/slab entropies in  $D = 4, 5$ , especially the difference between orientations parallel and transverse to the vector condensate.

We keep the visible  $p$ -wave system fixed and add hidden sectors to it. Thus the actions considered below should be read as

$$S_{\text{tot}}^{(i)} = S_{\text{bg}} + S_{\text{vis}} + \Delta S_{\text{dark}}^{(i)}, \quad (1.1)$$

not as replacements for the visible Yang-Mills theory. The visible ansatz is

$$B^a \tau^a = b(u) \tau^3 dt + \omega(u) \tau^1 dx_1. \quad (1.2)$$

Here  $b(u)$  fixes the grand-canonical source,  $b(u \rightarrow \infty) = \sqrt{3} \mu$ , and regularity sets  $b(1) = 0$  at the horizon. The function  $\omega(u)$  is the radial profile of the  $p$ -wave order parameter. A source-free ordered branch is obtained by solving the coupled Euler-Lagrange equations for  $b$  and  $\omega$  with the

non-normalizable part of  $\omega$  set to zero. The Sturm-Liouville problem is introduced only after this step, by linearising the same equations as  $\omega = \epsilon\psi + O(\epsilon^3)$  near the critical point.

This ordering is important for the present paper. A dark deformation can change the temporal equation for  $b$ , the spatial equation for  $\omega$ , or both. Therefore we first derive the radial equations of motion for the visible problem and then repeat the derivation after each hidden-sector term is added. Only afterwards do we extract the critical chemical potential from the linearized equation and compare the branch grand potentials. This follows the standard logic of holographic superconductors and anisotropic superfluids: model and ansatz, radial equations, numerical profiles for  $b$  and  $\omega$ , critical point, and finally free-energy or entanglement checks [53, 54, 55, 56, 57, 15, 58, 39].

The hidden-sector deformations studied here fall into three classes. Case I contains temporal hidden gauge fields. Case II is a hidden-SU(2) kinetic-mixing system; without an independent hidden chemical potential it gives an exact square-root reduction of the visible critical chemical potential. Case III adds a hidden dark singlet scalar  $\Phi$ , dual to a dark scalar boundary operator  $\mathcal{O}_\Phi$ , coupled to the visible sector only through a portal. A mass portal  $\lambda_\Phi\Phi^2B^2$  (Case III-a) adds an isotropic cost that raises the critical chemical potential. A kinetic portal  $Z_{\text{dm}}(\Phi)G^2$  (Case III-b) instead changes both the normal-branch temporal profile and the spatial vector zero mode. Its critical-point shift is therefore background dependent rather than a universal lowering or raising. These dark-scalar portals are used as representative settings for the competition between an isotropic scalar channel, the anisotropic  $p$ -wave channel, and coexistence.

The dimension coverage is intentionally asymmetric. The analytic reference point  $d(1 + \theta) = 3$ ,  $z = 1$  contains the AdS<sub>5</sub> point  $(D, \theta, z) = (5, 0, 1)$  and the hyperscaling-violating islands  $(4, 1/2, 1)$  and  $(3, 2, 1)$ . The  $D = 4$  island is singled out whenever we discuss the exact reduced law with an independently sourced hidden chemical potential. The  $D = 5$  sector contains the full hyperscaling-violating linearized survey, the tensor-portal relative-shift grid, and the representative mixed-branch calculation. We do not claim a fully back-reacted global phase diagram over the whole  $(D, z, \theta)$  space.

The organization is as follows. Section 2 fixes the radial coordinate and derives the visible and dark-deformed equations of motion for  $b$  and  $\omega$ . Section 3 reviews the visible HSV critical point and gives a general operator-level account of dark response; the hidden-SU(2) square-root law is treated there only as one solvable benchmark. Section 4 defines the HEE observables, the null-channel source rules, and the tensor-portal susceptibility as a linear-response coefficient before explaining the first-law and condensate checks. Section 5 then presents the results in the order dictated by the physics: the strip-difference selection rule, the tensor-portal susceptibility and its short-distance decoupling, the HSV-dependent critical-scale shift, and the radial-profile mechanism. Appendix A collects supporting plots, and Sec. 6 summarizes the scope of the result.

## 2 Model and equations of motion

This section fixes the undeformed holographic model before any hidden sector is added. We first write the complete Einstein–dilaton– $U(1)$ –SU(2) action and its Euler–Lagrange equations. We then insert the HSV black-brane background and the visible  $p$ -wave ansatz. The dark sectors are introduced

only afterwards, as deformations of the same Yang–Mills equations. This order is important: the critical-point problem is not postulated as a Sturm–Liouville equation; it is obtained by linearising the explicit radial Yang–Mills equations around the isotropic normal branch.

## 2.1 Visible sector: Anisotropic holographic superfluid

The undeformed theory on which all dark-sector cases are built is

$$S_0 = \frac{1}{\kappa_D^2} \int d^D x \sqrt{-g} \left[ R - \frac{1}{2} g^{MN} \partial_M \phi \partial_N \phi + V_0 e^{\gamma \phi} - \frac{\kappa_D^2}{4g_U^2} e^{\lambda_U \phi} F_{MN} F^{MN} - \frac{\kappa_D^2}{4g_{\text{YM}}^2} e^{\lambda_{\text{YM}} \phi} G_{MN}^a G^{aMN} \right], \quad (2.1)$$

where  $D = d + 2$ ,  $M, N = 0, \dots, D - 1$ , and  $d$  is the number of boundary spatial directions. The Abelian and non-Abelian field strengths are

$$F_{MN} = \partial_M A_N - \partial_N A_M, \quad G_{MN}^a = \partial_M B_N^a - \partial_N B_M^a - \epsilon^{abc} B_M^b B_N^c, \quad (2.2)$$

with  $B = B_M^a \tau^a dx^M$ ,  $[\tau^a, \tau^b] = i\epsilon^{abc} \tau^c$ , and  $\text{Tr}(\tau^a \tau^b) = \delta^{ab}/2$ .

Varying (2.1) gives four sets of bulk equations. The scalar equation is

$$\mathcal{X} \equiv \frac{1}{\sqrt{-g}} \partial_M (\sqrt{-g} g^{MN} \partial_N \phi) + \gamma V_0 e^{\gamma \phi} - \frac{\kappa_D^2 \lambda_U}{4g_U^2} e^{\lambda_U \phi} F_{MN} F^{MN} - \frac{\kappa_D^2 \lambda_{\text{YM}}}{4g_{\text{YM}}^2} e^{\lambda_{\text{YM}} \phi} G_{MN}^a G^{aMN} = 0. \quad (2.3)$$

The Maxwell equation is

$$\mathcal{Y}_U^N \equiv \frac{1}{\sqrt{-g}} \partial_M (\sqrt{-g} e^{\lambda_U \phi} F^{MN}) = 0, \quad (2.4)$$

and the visible Yang–Mills equation is

$$\mathcal{Y}_{\text{YM}}^{aN} \equiv \frac{1}{\sqrt{-g}} \partial_M (\sqrt{-g} e^{\lambda_{\text{YM}} \phi} G^{aMN}) + e^{\lambda_{\text{YM}} \phi} \epsilon^{abc} G^{bMN} B_M^c = 0. \quad (2.5)$$

Finally, the trace-reversed Einstein equation is

$$\begin{aligned} \mathcal{W}_{MN} \equiv & R_{MN} - \frac{1}{2} \partial_M \phi \partial_N \phi + \frac{1}{D-2} V_0 e^{\gamma \phi} g_{MN} \\ & - \frac{\kappa_D^2}{2g_U^2} e^{\lambda_U \phi} \left( F_{MP} F_N^P - \frac{1}{2(D-2)} g_{MN} F_{PQ} F^{PQ} \right) \\ & - \frac{\kappa_D^2}{2g_{\text{YM}}^2} e^{\lambda_{\text{YM}} \phi} \left( G_{MP}^a G_N^a{}^P - \frac{1}{2(D-2)} g_{MN} G_{PQ}^a G^{aPQ} \right) = 0. \end{aligned} \quad (2.6)$$

Equations (2.3)–(2.6) are the original equations before any dark-sector deformation is introduced.

The isotropic HSV black-brane seed is obtained from the ansatz

$$ds^2 = r_h^{2\theta} u^{2\theta} \left[ -u^{2z} f(u) dt^2 + \frac{du^2}{u^2 f(u)} + u^2 \delta_{ij} dx^i dx^j \right], \quad u \equiv \frac{r}{r_h}, \quad (2.7)$$

with horizon  $u = 1$ , boundary  $u \rightarrow \infty$ , and

$$f(u) = 1 - u^{-n_h}, \quad n_h = d\theta + z + d. \quad (2.8)$$

The dilaton profile and the EMD couplings are fixed by the HSV equations:

$$\phi(u) = \phi_0 + \sqrt{2d(1+\theta)(\theta+z-1)} \ln u, \quad (2.9)$$

$$\lambda_{\text{YM}} = \sqrt{\frac{2(\theta+z-1)}{d(1+\theta)}}, \quad \gamma = -\frac{2\theta}{\sqrt{2d(1+\theta)(\theta+z-1)}}, \quad (2.10)$$

$$\lambda_U = -\frac{2\theta(d-1)+2d}{\sqrt{2d(1+\theta)(\theta+z-1)}}, \quad V_0 = e^{-\gamma\phi_0}(d\theta+z+d-1)(d\theta+z+d). \quad (2.11)$$

In the probe computations below the background SU(2) charge term in  $f(u)$  is dropped by taking  $\kappa_D^2/g_{\text{YM}}^2 \rightarrow 0$ ; the visible Yang–Mills fields are then solved on the fixed HSV geometry.

The null-energy condition is not an additional numerical assumption. It is the algebraic condition obtained by contracting the Einstein equation with independent null vectors of the HSV metric. Let

$$k_{(1)}^M = (\sqrt{g^{uu}}, \sqrt{-g^{tt}}, 0, \dots, 0), \quad k_{(2)}^M = (0, \sqrt{-g^{tt}}, \sqrt{g^{x_1x_1}}, 0, \dots, 0), \quad (2.12)$$

which satisfy  $g_{MN}k_{(i)}^M k_{(i)}^N = 0$ . Since the potential term is proportional to  $g_{MN}$ , it drops out after contraction with a null vector. Using (2.6), the two independent NEC contractions reduce to the Ricci differences

$$T_{MN}k_{(1)}^M k_{(1)}^N \geq 0 \iff R^u{}_u - R^t{}_t = d(1+\theta)(\theta+z-1)u^{-2\theta}f(u) \geq 0, \quad (2.13)$$

$$T_{MN}k_{(2)}^M k_{(2)}^N \geq 0 \iff R^{x_1}{}_{x_1} - R^t{}_t = (z-1)[z+d(1+\theta)]u^{-2\theta} \geq 0. \quad (2.14)$$

Outside the horizon  $f(u) > 0$ . Thus the allowed HSV domain is

$$(1+\theta)(\theta+z-1) \geq 0, \quad (z-1)[z+d(1+\theta)] \geq 0. \quad (2.15)$$

The surveys in this paper use  $z \geq 1$  and  $\theta \geq 0$ , so both inequalities are automatically satisfied; points outside (??) are not used in the numerical scans.

The inverse metric components entering the Yang–Mills radial reduction are

$$g^{uu} = r_h^{-2\theta}u^{-2\theta}u^2f(u), \quad g^{tt} = -r_h^{-2\theta}u^{-2\theta}u^{-2z}f(u)^{-1}, \quad g^{x_ix_i} = r_h^{-2\theta}u^{-2\theta}u^{-2}. \quad (2.16)$$

The overall powers of  $r_h$  set dimensions and will be suppressed in the dimensionless radial equations below.

## 2.2 Visible SU(2) Yang–Mills sector

The visible gauge field is an SU(2) connection  $B = B_M^a \tau^a dx^M$  with field strength

$$G_{MN}^a = \partial_M B_N^a - \partial_N B_M^a - \epsilon^{abc} B_M^b B_N^c, \quad (2.17)$$

and the Yang–Mills action is

$$S_{\text{vis}} = -\frac{1}{4g_{\text{YM}}^2} \int d^{d+2}x \sqrt{-g} e^{\lambda_{\text{YM}}\phi} G_{MN}^a G^{aMN}. \quad (2.18)$$

The  $p$ -wave ansatz is

$$B^a \tau^a = b(u)\tau^3 dt + \omega(u)\tau^1 dx_1. \quad (2.19)$$

Substituting (2.19) into (2.17), the non-vanishing radial field-strength components are

$$G_{ut}^3 = b'(u), \quad G_{ux_1}^1 = \omega'(u), \quad G_{tx_1}^2 = -b(u)\omega(u), \quad (2.20)$$

where a prime denotes  $d/du$ . Contracting with the inverse metric gives a one-dimensional radial functional. It is useful not to quote the determinant alone, because the only invariant data entering the fluctuation problem are the products  $\sqrt{-g} e^{\lambda_{\text{YM}}\phi} g^{MM} g^{NN}$ . In the radial gauge and normalisation used throughout the numerical evidence pack, these products are fixed by the HSV background and reduce to the weights displayed below. The quadratic Yang–Mills Lagrangian density is

$$\mathcal{L}_{\text{YM}}^{(1d)} = -\frac{1}{2}[\mathcal{P}_b(u) b'^2 + \mathcal{P}_\omega(u) \omega'^2 + \mathcal{M}(u) b^2 \omega^2], \quad (2.21)$$

where we define, up to an overall positive constant independent of  $u$ ,

$$\mathcal{P}_b(u) \equiv \sqrt{-g} e^{\lambda_{\text{YM}}\phi} (-g^{uu}) (-g^{tt}) = u^{d(1+\theta)+z-1}, \quad (2.22)$$

$$\mathcal{P}_\omega(u) \equiv \sqrt{-g} e^{\lambda_{\text{YM}}\phi} g^{uu} g^{x_1 x_1} = u^{n_p} f(u), \quad n_p \equiv d\theta + d + 3z - 3, \quad (2.23)$$

$$\mathcal{M}(u) \equiv \sqrt{-g} e^{\lambda_{\text{YM}}\phi} (-g^{tt}) g^{x_1 x_1} = \frac{u^{n_h-5}}{f(u)}. \quad (2.24)$$

Equations (2.22)–(2.24) are the explicit radial reduction used in the eigenvalue problem. For example,  $\mathcal{P}_\omega$  is the coefficient of the spatial gauge kinetic term  $G_{ux_1}^1 G^{1ux_1}$ ; after inserting the HSV solution and the dilaton coupling, the power of  $u$  is  $n_p = d\theta + d + 3z - 3$ , while the horizon zero comes entirely from the factor  $g^{uu} \propto f$ . The electric weight  $\mathcal{M}$  instead contains  $(-g^{tt}) \propto f^{-1}$ , which is why it carries the reciprocal horizon factor.

The Euler–Lagrange equations obtained from varying  $b$  and  $\omega$  in the one-dimensional action  $I_{\text{YM}}^{(1d)} = \int du \mathcal{L}_{\text{YM}}^{(1d)}$  are

$$\partial_u(\mathcal{P}_b b') - \mathcal{M} b \omega^2 = 0, \quad (2.25)$$

$$\partial_u(\mathcal{P}_\omega \omega') + \mathcal{M} b^2 \omega = 0. \quad (2.26)$$

Equations (2.25) and (2.26) are the equations solved for the radial profiles. In a numerical shooting or boundary-value formulation one imposes regular horizon data

$$b(1) = 0, \quad \omega(1) = \omega_h, \quad (2.27)$$

with the first derivatives fixed by the regular near-horizon expansion. At the boundary the grand-canonical ensemble fixes

$$b(u) = \sqrt{3} \mu - \rho_b u^{-(n_h-2)} + \dots, \quad \omega(u) = \omega_{\text{src}} + \omega_{\text{vev}} u^{-(n_p-1)} + \dots, \quad (2.28)$$

where the source-free  $p$ -wave branch has  $\omega_{\text{src}} = 0$  and  $\omega_{\text{vev}} \propto \langle J_{x_1}^1 \rangle$ . Thus the functions  $b(u)$  and  $\omega(u)$  are obtained directly from the Euler–Lagrange equations. The Sturm–Liouville method enters only after expanding these same equations around the isotropic solution.

Near the linearised critical point we write

$$b(u) = b_0(u) + O(\epsilon^2), \quad \omega(u) = \epsilon \psi(u) + O(\epsilon^3), \quad (2.29)$$

where  $b_0$  is the source-free isotropic temporal profile

$$b_0(u) = \sqrt{3}\mu(1 - u^{-(n_h-2)}), \quad (2.30)$$

satisfying  $b_0(1) = 0$  and  $b_0(u) \rightarrow \sqrt{3}\mu$  as  $u \rightarrow \infty$ . At leading order,  $\psi$  obeys the Sturm–Liouville equation

$$\boxed{\partial_u [P(u) \psi'(u)] + Q(u; \mu) \psi(u) = 0}, \quad (2.31)$$

with

$$P(u) = u^{n_p}(1 - u^{-n_h}), \quad Q(u; \mu) = 3\mu^2 \frac{u^{n_h-5}(1 - u^{-(n_h-2)})^2}{1 - u^{-n_h}}. \quad (2.32)$$

The critical chemical potential  $\mu_c(d, z, \theta)$  is the smallest  $\mu$  for which (2.31) has a normalizable solution with vanishing source at  $u \rightarrow \infty$ . At the analytic reference point  $d(1 + \theta) = 3$ ,  $z = 1$ , one has  $n_h = 4$ ,  $n_p = 3$ , and the closed-form zero mode

$$\psi_0(u) = \frac{u^2}{(1 + u^2)^2}, \quad \mu_c = \frac{4}{\sqrt{3}}. \quad (2.33)$$

### 2.2.1 Thermodynamic meaning of the reference transition

The normal branch has  $\omega = 0$  and is spatially isotropic. A source-free normalizable solution of Eq. (2.31) is the linear critical point of the  $p$ -wave branch; in the boundary theory this is the transition to a phase with vector order parameter  $\langle J_{x_1}^1 \rangle \neq 0$ . We use the grand-potential criterion of Park–Park–Oh: if

$$\Delta\Omega \equiv \Omega_{\omega \neq 0} - \Omega_{\omega=0} < 0, \quad (2.34)$$

then the anisotropic phase is thermodynamically favoured at the same boundary chemical potential.

The perturbative branch expansion is most transparent in the inverse radial coordinate  $\xi = 1/u$ . Let

$$\omega(\xi) = \epsilon \psi_1(\xi) + O(\epsilon^3), \quad b(\xi) = b_0(\xi) + \epsilon^2 \beta_2(\xi) + O(\epsilon^4), \quad (2.35)$$

with  $\beta_2(0) = \beta_2(1) = 0$ . The order- $\epsilon^2$  temporal backreaction solves

$$\partial_\xi [K_b(\xi) \partial_\xi \beta_2] = M(\xi) b_0(\xi) \psi_1^2(\xi), \quad K_b(\xi) = \xi^{-d\theta-z}. \quad (2.36)$$

For the source-free branch comparison at the same boundary chemical potential,

$$\Delta\Omega_{A|N} = -\epsilon^4 \int_0^1 d\xi K_b(\xi) (\partial_\xi \beta_2)^2 + O(\epsilon^6) < 0, \quad (2.37)$$

whenever the local branch exists. This is the reference thermodynamic sign used below. It should not be confused with a finite-amplitude attempt to draw a pure-visible ordered–ordered boundary  $z_*(\theta)$ . The controlled dark-sector observable in this paper is the critical surface  $\mu_c$  and the associated near-critical branch energetics.

Every dark-sector deformation below modifies (2.31); the key question is whether the modification changes only the eigenvalue  $\mu_c$  or also the structure of the operator.

### 2.3 General dark-sector deformations of the Yang–Mills equations

We now add dark sectors to the same undeformed action (2.1). The bookkeeping is

$$S_{\text{tot}}^{(i)} = S_0 + \Delta S_{\text{dark}}^{(i)}, \quad (2.38)$$

where  $S_0$  already contains the visible  $SU(2)$  field  $B_M^a$ . The cases below differ only in the additional term  $\Delta S_{\text{dark}}^{(i)}$ . In each case we display the deformation of the same two visible radial equations,

$$\partial_u(\mathcal{P}_b b') - \mathcal{M} b \omega^2 = 0, \quad \partial_u(\mathcal{P}_\omega \omega') + \mathcal{M} b^2 \omega = 0, \quad (2.39)$$

rather than introducing a new critical equation by hand. Schematically, a general dark deformation changes these equations to

$$\partial_u(\mathcal{P}_b^{\text{eff}} b' + \mathcal{P}_{bX}^{\text{eff}} X') - \mathcal{M}_{\text{eff}} b \omega^2 + \dots = 0, \quad (2.40)$$

$$\partial_u(\mathcal{P}_\omega^{\text{eff}} \omega') + \mathcal{Q}_{\text{eff}}(u; b, X, \Phi) \omega = 0. \quad (2.41)$$

The dots denote possible scalar or hidden-gauge source terms. The linear critical problem is obtained from (2.41) by setting  $b = b_0 + O(\omega^2)$  and keeping the term linear in  $\omega$ . The nonlinear branch and the grand potential require the full radial system.

It is useful to distinguish the visible order parameter from the dark sector. The  $SU(2)$  Yang–Mills field  $B_M^a$  is the visible sector in our terminology:  $B_t^3 = b(u)$  defines the visible chemical potential and  $B_{x_1}^1 = \omega(u)$  is the vector order parameter responsible for the anisotropic phase. Cases I and II add hidden gauge fields: an Abelian field  $X_M$  and a second non-Abelian field  $C_M^a$ . Cases III-a and III-b add a hidden dark scalar  $\Phi$ , dual to a dark scalar operator  $\mathcal{O}_\Phi$ , which is neutral under the visible  $SU(2)$ . Neutral here means only that  $\Phi$  carries no visible flavor charge; it does *not* mean that the scalar is a visible-sector deformation. It is an independent dark-sector field, and its only communication with the visible  $p$ -wave system is through portal couplings.

We use  $\alpha_{\text{dm}}$  as the dark-sector portal strength throughout the paper, with the precise operator depending on the case. In the hidden-gauge cases it is the usual kinetic-mixing parameter. In the dark-scalar cases it multiplies the scalar portal,

$$\Delta S_{\text{dark}}^{\text{III-a}} = - \int d^{d+2} x \sqrt{-g} \alpha_{\text{dm}}^2 \lambda_\Phi \Phi^2 B_M^a B^{aM}, \quad Z_{\text{dm}}(\Phi) = 1 + \alpha_{\text{dm}}^2 \beta \Phi^2 + \dots \quad (2.42)$$

Thus the scalar cases remain dark-sector deformations in the same sense as the hidden gauge cases: a field outside the visible  $SU(2)$  order-parameter sector modifies the visible current operator through a controlled portal. In numerical plots of the dark-scalar portals we absorb the fixed value of  $\alpha_{\text{dm}}$  into the effective combinations  $\alpha_{\text{dm}} \Phi_h$ ,  $\alpha_{\text{dm}}^2 \lambda_\Phi \Phi_h^2$ , and  $\alpha_{\text{dm}}^2 \beta \Phi_h^2$ . This avoids introducing a second notation for the same dark-sector strength while keeping the hidden-gauge and hidden-scalar mechanisms distinct.

The four deformations are chosen to span the minimal ways in which a dark sector outside the visible  $p$ -wave order parameter can affect the HSV superfluid.

- Case I represents the simplest hidden Abelian current sector. It tests whether an additional  $U(1)_X$  charge sector, coupled only through the dark portal and backreaction, can modify the visible critical point and geometric response without introducing a second vector order parameter.

- Case II represents a genuinely non-Abelian hidden sector. Since the hidden field  $C_M^a$  has the same adjoint structure as the visible  $SU(2)$  field  $B_M^a$ , this case gives the cleanest test of hidden non-Abelian kinetic mixing and leads to the exact rescaling structure controlled by  $1 - \alpha_{\text{dm}}^2/4$ .
- Case III-a is a hidden dark scalar with an  $\alpha_{\text{dm}}$ -controlled mass portal. Being isotropic, it tests whether a dark scalar environment that raises the visible-vector cost without selecting a spatial direction can affect the leading anisotropic HEE response.
- Case III-b is the kinetic portal of the same hidden dark scalar. The color-blind factor  $Z_{\text{dm}}(\Phi(u))$  reweights the visible current operator radially, so it shifts the critical point by a profile-dependent amount and generates a non-null geometric response. It is the dark-scalar counterpart of hidden gauge mixing.

### 2.3.1 Case I: temporal hidden $U(1)$ gauge sector

The simplest dark extension adds a hidden Abelian gauge field  $X_M$  with field strength

$$X_{MN} = \partial_M X_N - \partial_N X_M \quad (2.43)$$

and a kinetic-mixing portal with the visible color-3 electric field:

$$\Delta S_X = -\frac{1}{4} \int d^D x \sqrt{-g} [Z_X(\phi) X_{MN} X^{MN} + 2\chi Z_m(\phi) G_{MN}^3 X^{MN}]. \quad (2.44)$$

The full action is  $S_{\text{tot}}^{(X)} = S_0 + \Delta S_X$ . With the temporal ansatz

$$X = x(u)dt, \quad X_{ut} = x'(u), \quad (2.45)$$

the radial electric weights are

$$\mathcal{P}_X(u) = \sqrt{-g} Z_X(\phi) (-g^{uu} g^{tt}), \quad \mathcal{P}_m(u) = \sqrt{-g} Z_m(\phi) (-g^{uu} g^{tt}). \quad (2.46)$$

The temporal equations are no longer the undeformed visible equation  $\partial_u(\mathcal{P}_b b') - \mathcal{M}b\omega^2 = 0$ . They become

$$\partial_u[\mathcal{P}_b b' + \chi \mathcal{P}_m x'] - \mathcal{M}b\omega^2 = 0, \quad (2.47)$$

$$\partial_u[\mathcal{P}_X x' + \chi \mathcal{P}_m b'] = 0. \quad (2.48)$$

The spatial visible equation is still

$$\partial_u(\mathcal{P}_\omega \omega') + \mathcal{M}b^2\omega = 0. \quad (2.49)$$

Thus Case I changes the temporal electric sector, and therefore the relation between the boundary chemical potentials and the radial profile  $b(u)$ . It does *not* introduce a new direct mass term for  $\omega$  at the linear probe level. If the hidden Abelian field is kept probe and the HSV geometry is fixed, the source-free vector operator is the same as the visible one after the appropriate temporal solution  $b_0(u)$  has been chosen.

### 2.3.2 Case II: hidden SU(2) with kinetic mixing

We introduce a second SU(2) connection  $C_M^a \tau^a$  with field strength  $H_{MN}^a$ , coupled to the visible sector through a kinetic-mixing parameter  $\alpha_{\text{dm}}$ . The gauge-sector part of the action is

$$S_{\text{vis+dark}} = -\frac{1}{4} \int d^{d+2}x \sqrt{-g} e^{\lambda_{\text{YM}}\phi} (G_{MN}^a G^{aMN} + H_{MN}^a H^{aMN} + \alpha_{\text{dm}} G_{MN}^a H^{aMN}), \quad (2.50)$$

The total action is obtained from  $S_0$  by replacing the visible  $G^2$  gauge-sector term in (2.1) with the bracket in (2.50). Equivalently, the gauge sector is  $S_{\text{vis}} + S_H + S_{\text{mix}}$ ; the visible  $G^2$  term is still present. We take the dark temporal ansatz  $C^a \tau^a = \eta(u) \tau^3 dt$ , so that  $H_{ut}^3 = \eta'(u)$  and all other components vanish.

**Temporal equations.** The original visible temporal equation  $\partial_u(\mathcal{P}_b b') - \mathcal{M} b \omega^2 = 0$  is deformed already before the spatial fluctuation is considered. Varying (2.50) with respect to  $b$  and  $\eta$  gives

$$\partial_u \left[ \mathcal{P}_b(u) \left( b' + \frac{\alpha_{\text{dm}}}{2} \eta' \right) \right] - \mathcal{M}(u) b \omega^2 = 0, \quad (2.51)$$

$$\partial_u \left[ \mathcal{P}_b(u) \left( \eta' + \frac{\alpha_{\text{dm}}}{2} b' \right) \right] = 0. \quad (2.52)$$

In the normal branch,  $\omega = 0$ , the second equation integrates to

$$\eta'(u) + \frac{\alpha_{\text{dm}}}{2} b'_0(u) = \frac{Q_X}{\mathcal{P}_b(u)}. \quad (2.53)$$

The integration constant  $Q_X$ , together with the additive gauge constant, fixes the independent hidden chemical potential. For the minimal ensemble with no independent hidden source,  $Q_X = 0$ , and hence

$$\eta(u) = -\frac{\alpha_{\text{dm}}}{2} b_0(u) + c_X. \quad (2.54)$$

In the boundary-source convention used for the two-parameter critical surface one writes  $c_X = \mu_X + \alpha_{\text{dm}} \sqrt{3} \mu / 2$ , so that the independent source is  $\mu_X$ . In the horizon-regular profile convention used for the radial-profile checks, one instead sets  $c_X = 0$ , and the induced dark profile is simply  $\eta = -\alpha_{\text{dm}} b_0 / 2$ .

**Visible  $\omega$ -equation with mixing.** The coupled visible Yang–Mills equations obtained by varying  $B_M^a$  in (2.50) are

$$\nabla_M G^{aMN} + \frac{\alpha_{\text{dm}}}{2} \nabla_M H^{aMN} + \epsilon^{abc} B_M^b (G^{cMN} + \frac{\alpha_{\text{dm}}}{2} H^{cMN}) = 0, \quad (2.55)$$

$$\nabla_M H^{aMN} + \frac{\alpha_{\text{dm}}}{2} \nabla_M G^{aMN} + \epsilon^{abc} C_M^b (H^{cMN} + \frac{\alpha_{\text{dm}}}{2} G^{cMN}) = 0. \quad (2.56)$$

Substituting  $N = x_1$  and  $a = 1$  in (2.55), using  $H^{1Mx_1} = 0$  (since  $\eta$  has only  $a = 3$ ), the structure-constant terms yield

$$\epsilon^{132} B_t^3 G^{2tx_1} + \frac{\alpha_{\text{dm}}}{2} \epsilon^{132} C_t^3 G^{2tx_1} = -(b_0 + \frac{\alpha_{\text{dm}}}{2} \eta) (-b_0 \omega) (-g^{tt} g^{x_1 x_1}). \quad (2.57)$$

The elimination is elementary but important, so we spell it out. In the  $N = x_1$ ,  $a = 1$  sector the two radial kinetic equations have the schematic matrix form

$$\begin{pmatrix} 1 & \alpha_{\text{dm}}/2 \\ \alpha_{\text{dm}}/2 & 1 \end{pmatrix} \begin{pmatrix} \nabla_M G^{1Mx_1} \\ \nabla_M H^{1Mx_1} \end{pmatrix} = \begin{pmatrix} \mathcal{J}_G \\ \mathcal{J}_H \end{pmatrix}, \quad \det = 1 - \frac{\alpha_{\text{dm}}^2}{4} \equiv \tilde{\alpha}. \quad (2.58)$$

Multiplying the first row by one and subtracting  $\alpha_{\text{dm}}/2$  times the second row gives

$$\tilde{\alpha} \nabla_M G^{1Mx_1} = \mathcal{J}_G - \frac{\alpha_{\text{dm}}}{2} \mathcal{J}_H. \quad (2.59)$$

Thus the visible kinetic operator is multiplied by  $\tilde{\alpha} = 1 - \alpha_{\text{dm}}^2/4$ , while the source terms generate the mixed radial contribution proportional to  $\eta b_0 \omega$ . The full reduced  $\omega$ -equation is

$$\partial_u(P \psi') + \frac{1}{\tilde{\alpha}} Q_{\text{vis}}(u; \mu) \psi - \frac{\alpha_{\text{dm}}^2}{4\tilde{\alpha}} Q_{\text{mix}}(u) \psi = 0, \quad (2.60)$$

with

$$\tilde{\alpha} \equiv 1 - \frac{\alpha_{\text{dm}}^2}{4}, \quad Q_{\text{mix}}(u) \equiv \frac{u^{n_h-5} \eta(u) b_0(u)}{1 - u^{-n_h}}. \quad (2.61)$$

The special subfamily used for the exact scaling law is the minimal kinetic-mixing ensemble with no independent dark temporal source. It is important to obtain the reduced equation correctly. One cannot simply substitute the induced profile  $\eta = -\alpha_{\text{dm}} b_0/2$  into (2.60) and set the hidden spatial mode to zero: the off-diagonal kinetic term sources  $C_{x_1}^1$ , so the hidden spatial fluctuation does not vanish and must be *eliminated* rather than dropped. The clean way to perform this elimination is to diagonalise the quadratic mixed gauge action. Writing the symmetric kinetic matrix of  $(G_{MN}^a, H_{MN}^a)$  as

$$\mathbb{K} = \begin{pmatrix} 1 & \alpha_{\text{dm}}/2 \\ \alpha_{\text{dm}}/2 & 1 \end{pmatrix}, \quad \det \mathbb{K} = 1 - \frac{\alpha_{\text{dm}}^2}{4} = \tilde{\alpha}, \quad (2.62)$$

the rotation  $G_{\pm} = (G \pm H)/\sqrt{2}$  diagonalises it with eigenvalues  $1 \pm \alpha_{\text{dm}}/2$ . With no independent hidden source the hidden channel carries no free boundary data, so integrating it out of the quadratic action multiplies the visible current inverse two-point operator by the single factor  $\det^{-1} \mathbb{K} = 1/\tilde{\alpha}$ . Equivalently, the visible zero-mode equation depends on the chemical potential only through the renormalised combination  $\hat{\mu}^2 = \mu^2/\tilde{\alpha}$ , and the source-free spatial equation collapses to the *pure rescaling form*

$$\partial_u(P \psi') + \frac{\mu^2}{\tilde{\alpha}} W_0(u) \psi = 0, \quad (2.63)$$

where  $W_0(u) = Q_{\text{vis}}(u; \mu)/\mu^2$  is the  $\mu$ -independent electric weight function of the undeformed problem. The boxed equation (2.60) is the general single-channel form retained for the non-minimal case; its reduction to (2.63) is the elimination just described, and is verified numerically to machine precision across the scanned  $(d, z, \theta)$  in Sec. 3. By contrast, when an independent hidden chemical potential is kept fixed, the hidden channel does carry free boundary data, the term  $Q_{\text{mix}}$  in (2.60) is no longer proportional to  $Q_{\text{vis}}$ , and the square-root scaling is no longer guaranteed. This separation between pure kinetic rescaling and genuine operator-shape deformation is the structural fact behind Section 3.

**Two-component spatial eigenproblem.** If both visible and hidden spatial fluctuations are allowed,  $B_{x_1}^1 = \omega_v(u)$  and  $C_{x_1}^1 = \omega_d(u)$ , the critical mode becomes a two-component vector

$$\Psi(u) = \begin{pmatrix} \omega_v(u) \\ \omega_d(u) \end{pmatrix}, \quad (2.64)$$

and the linearised problem takes the matrix Sturm–Liouville form

$$-\partial_u(\mathbb{P}(u) \partial_u \Psi) + \mathbb{V}(u) \Psi = \mu^2 \mathbb{W}(u) \Psi, \quad (2.65)$$

with  $2 \times 2$  coefficient matrices  $\mathbb{P}$ ,  $\mathbb{V}$ ,  $\mathbb{W}$  whose off-diagonal entries are proportional to  $\alpha_{\text{dm}}$ . The composition of the lowest eigenmode is measured by the fractions

$$f_v = \frac{\int du \mathcal{W}_v \omega_v^2}{\int du (\mathcal{W}_v \omega_v^2 + \mathcal{W}_d \omega_d^2)}, \quad f_d = 1 - f_v, \quad (2.66)$$

with the positive radial weight from the quadratic fluctuation norm. A lower eigenvalue with  $f_d \rightarrow 1$  is a dark-dominated instability, not a visible  $p$ -wave transition.

### 2.3.3 Case III-a: hidden dark scalar with a mass portal

Cases I and II add a second *gauge* sector. Case III instead adds a hidden *dark scalar*  $\Phi$ . The scalar is neutral under the visible  $SU(2)$ , so it has no adjoint covariant derivative and no visible flavor charge, but it is not part of the visible sector. On the boundary it is dual to a dark scalar operator  $\mathcal{O}_\Phi$ , and it communicates with the visible  $p$ -wave sector only through the  $\alpha_{\text{dm}}$ -controlled portal in Eq. (2.42). Its own action is

$$S_\Phi = - \int d^{d+2} x \sqrt{-g} \left[ \frac{1}{2} g^{MN} \partial_M \Phi \partial_N \Phi + V(\Phi) \right], \quad V(\Phi) = \frac{1}{2} m_\Phi^2 \Phi^2 + \dots, \quad (2.67)$$

so that  $\Phi$  obeys the scalar equation

$$\partial_u(\sqrt{-g} g^{uu} \Phi') - \sqrt{-g} m_\Phi^2 \Phi = 0, \quad (2.68)$$

with *no*  $\epsilon^{abc} B^b \Phi^c$  adjoint coupling. The profile  $\Phi(u)$  carries the two falloffs of the dark scalar operator; the dark-sector amplitude is fixed by its normalizable coefficient. Throughout the main susceptibility calculation we use representative normalizable backgrounds  $\Phi(u) = \Phi_h u^{-\Delta_\Phi}$ . This keeps the dark scalar sector prescribed and controlled; a fully dynamical scalar background is left outside the scope of the present probe analysis.

The Case III-a portal is a mass-type coupling between the singlet and the visible gauge field,

$$S_{\text{portal}}^{(a)} = - \int d^{d+2} x \sqrt{-g} \alpha_{\text{dm}}^2 \lambda_\Phi \Phi^2 B_M^a B^{aM}. \quad (2.69)$$

For the  $p$ -wave ansatz  $B_M^a B^{aM} = g^{tt} b^2 + g^{x_1 x_1} \omega^2$ , so the portal contributes an *isotropic* positive mass. The visible radial equations become

$$\partial_u(\mathcal{P}_b b') - \mathcal{M} b \omega^2 = 0, \quad (2.70)$$

$$\partial_u(\mathcal{P}_\omega \omega') + \mathcal{M} b^2 \omega - U_\Phi(u) \omega = 0, \quad U_\Phi(u) \equiv 2\alpha_{\text{dm}}^2 \lambda_\Phi \sqrt{-g} g^{x_1 x_1} \Phi(u)^2. \quad (2.71)$$

The added term is a positive mass for  $\omega$ , so the hidden scalar *raises* the critical chemical potential. Because  $\Phi$  is an isotropic singlet,  $U_\Phi$  is identical for every transverse orientation; the deformation is therefore null in the orientation-difference observable  $\mathcal{O}_{12}^{(2)}$  at leading order. Case III-a is thus a genuine *dark* deformation—a hidden dark operator  $\mathcal{O}_\Phi$  acting on the visible current sector—and not a scalar living inside the visible  $SU(2)$ .

### 2.3.4 Case III-b: hidden dark scalar with a kinetic portal (tensor portal)

Case III-b couples the same hidden singlet  $\Phi$  to the visible Yang–Mills kinetic term through a scalar-dependent prefactor,

$$S_{\text{portal}}^{(b)} = -\frac{1}{4} \int d^{d+2}x \sqrt{-g} Z_{\text{dm}}(\Phi) e^{\lambda_{\text{YM}}\phi} G_{MN}^a G^{aMN}, \quad Z_{\text{dm}}(\Phi) = 1 + \alpha_{\text{dm}}^2 \beta \Phi^2 + \dots \quad (2.72)$$

Since  $\Phi$  is a singlet,  $Z_{\text{dm}}(\Phi)$  is color-blind: it multiplies every color component of the field strength equally, so there is no adjoint  $Z_{\parallel}/Z_{\perp}$  splitting. The portal reweights the radial kinetic and electric terms by the common  $u$ -dependent factor  $Z_{\text{dm}}(\Phi(u))$ ,

$$\partial_u(Z_{\text{dm}}(\Phi) \mathcal{P}_b b') - Z_{\text{dm}}(\Phi) \mathcal{M} b \omega^2 = 0, \quad (2.73)$$

$$\partial_u(Z_{\text{dm}}(\Phi) \mathcal{P}_\omega \omega') + Z_{\text{dm}}(\Phi) \mathcal{M} b^2 \omega = 0. \quad (2.74)$$

At the normal branch,  $\omega = 0$ , the temporal equation must first be solved with the same kinetic factor. Writing the boundary value as  $b_\infty = \sqrt{3} \mu$ , the horizon-regular solution is

$$b_0^{(Z)}(u) = b_\infty \frac{\int_1^u \frac{dv}{Z_{\text{dm}}(\Phi(v)) \mathcal{P}_b(v)}}{\int_1^\infty \frac{dv}{Z_{\text{dm}}(\Phi(v)) \mathcal{P}_b(v)}} \equiv b_\infty \hat{b}_Z(u). \quad (2.75)$$

Thus the portal changes the shape of  $b_0$ ; keeping the visible power law while changing only the spatial equation would be inconsistent at the same order in the portal strength.

Linearising the spatial equation as  $\omega = \epsilon \psi + O(\epsilon^3)$  gives the self-adjoint problem

$$\partial_u [Z_{\text{dm}}(\Phi(u)) \mathcal{P}_\omega(u) \psi'(u)] + b_\infty^2 Z_{\text{dm}}(\Phi(u)) \mathcal{M}(u) \hat{b}_Z(u)^2 \psi(u) = 0. \quad (2.76)$$

The corresponding critical boundary amplitude is

$$b_{\infty,c}^2 = \min_{\psi_{\text{src}}=0} \frac{\int_1^\infty du Z_{\text{dm}}(\Phi) \mathcal{P}_\omega(\psi')^2}{\int_1^\infty du Z_{\text{dm}}(\Phi) \mathcal{M} \hat{b}_Z^2 \psi^2}, \quad \mu_c = \frac{b_{\infty,c}}{\sqrt{3}}. \quad (2.77)$$

Both the explicit factor  $Z_{\text{dm}}$  and the induced change of  $\hat{b}_Z$  enter the same eigenvalue problem. Consequently, the sign of the critical-point shift is not fixed by a simple numerator-versus-denominator argument. For the prescribed profile family used below, positive  $\beta$  raises  $\mu_c$  at the three analytic reference backgrounds, while the wider  $(\vartheta, z)$  scan contains regions in which the shift changes sign. The kinetic portal is non-null in  $\mathcal{O}_{12}^{(2)}$  because the same self-consistent  $b_0^{(Z)}$  and  $\psi_Z$  profiles change the traceless Yang–Mills source. The size of this effect is measured by the derivative susceptibility in Sec. 5.2.

## 3 Visible HSV scaling and dark-sector response

The purpose of this section is not to single out one hidden sector as the whole content of the paper. The exact hidden-SU(2) square-root law is only one analytically solvable benchmark. The broader

question is how the visible  $p$ -wave critical point, which already depends nontrivially on the HSV exponents, is modified when extra hidden gauge or scalar sectors deform the radial operator. We therefore proceed in three steps. First we recall the visible, dark-free scaling problem and explain how HSV geometry changes the critical scale relative to the isotropic AdS case. Second we write a general operator-level formula for how a dark deformation shifts the critical eigenvalue. Third we identify the minimal hidden-SU(2) case as the special subcase in which that general shift collapses to a closed square-root law.

### 3.1 Visible critical point before dark-sector deformation

Without any dark sector the source-free vector mode obeys the Sturm–Liouville problem (2.31). It is useful to rewrite it in the standard self-adjoint form

$$-\partial_u(P(u)\psi'(u)) = \mu^2 W_0(u)\psi(u), \quad W_0(u) \equiv \frac{Q(u; \mu)}{\mu^2}. \quad (3.1)$$

The corresponding Rayleigh quotient is

$$\mu_{c,\text{vis}}^2(d, z, \theta) = \min_{\psi_{\text{src}}=0} \frac{\int_1^\infty du P(u)(\psi')^2}{\int_1^\infty du W_0(u)\psi^2}. \quad (3.2)$$

This equation already contains the first scaling effect of the paper. In an isotropic AdS  $p$ -wave model one has  $z = 1$  and  $\theta = 0$ , so the powers entering  $P$  and  $W_0$  are fixed by the boundary dimension alone. In an HSV geometry these weights instead contain

$$n_h = d\theta + z + d, \quad n_p = d\theta + d + 3z - 3, \quad (3.3)$$

and therefore both the kinetic weight and the electric driving weight are reshaped by  $(z, \theta)$ . Thus even the visible theory has a nontrivial HSV critical point surface,

$$\mu_{c,\text{vis}} = \mu_{c,\text{vis}}(D, z, \theta), \quad (3.4)$$

rather than a single AdS critical number.

The physical transition scale follows from the horizon scaling. If  $\tilde{\mu}$  denotes the physical boundary chemical potential and  $\mu$  the dimensionless eigenvalue used in the radial problem, then

$$\tilde{\mu} \propto r_h^{n_h-2} \mu, \quad T = \frac{n_h}{4\pi} r_h^z. \quad (3.5)$$

At fixed physical chemical potential this gives, up to the same normalization used in the radial ansatz,

$$T_{c,\text{vis}}(D, z, \theta; \tilde{\mu}) = \frac{n_h}{4\pi} \left( \frac{\tilde{\mu}}{\mu_{c,\text{vis}}(D, z, \theta)} \right)^{z/(n_h-2)}. \quad (3.6)$$

Equation (3.6) is the baseline scaling law before any hidden deformation is added. The role of the dark sector is to replace  $\mu_{c,\text{vis}}$  by a deformed eigenvalue and, if the deformation changes the operator shape, to modify the radial profile that sources the HEE and probe free-energy checks.

### 3.2 General dark-sector deformation of the critical operator

A general dark deformation changes the self-adjoint problem in one of three ways:

$$P(u) \longrightarrow P(u) + \delta P(u), \quad W_0(u) \longrightarrow W_0(u) + \delta W(u), \quad U(u) \neq 0. \quad (3.7)$$

Here  $\delta P$  changes the radial kinetic weight of the vector zero mode,  $\delta W$  changes the electric driving weight, and  $U$  denotes an additional mass or cost term such as the scalar contribution generated by  $|D_{x_1} \Phi|^2$ . The deformed eigenvalue can be written as

$$\mu_c^2 = \min_{\psi_{\text{src}}=0} \frac{\int_1^\infty du [(P + \delta P)(\psi')^2 + U\psi^2]}{\int_1^\infty du (W_0 + \delta W)\psi^2}. \quad (3.8)$$

For a small deformation, evaluating the first variation on the undeformed normalizable zero mode  $\psi_0$  gives

$$\delta\mu_c^2 = \frac{\int_1^\infty du [\delta P(\psi_0')^2 + U\psi_0^2 - \mu_{c,\text{vis}}^2 \delta W \psi_0^2]}{\int_1^\infty du W_0 \psi_0^2} + O(\delta^2). \quad (3.9)$$

This formula is the useful organizing principle. A deformation that increases  $\delta P$  or adds a positive  $U$  tends to raise the critical point. A deformation that increases the electric driving weight  $\delta W$  tends to lower it. If the deformation is proportional to  $W_0$  everywhere, the shift is a global rescaling. If it is  $u$ -dependent, as in the tensor portal, the response is profile-dependent and cannot be reduced to one universal number.

The four cases of Sec. 2 occupy different positions in this operator language:

- **Case I** changes the temporal/electric sector through a hidden  $U(1)$  profile but does not add a new anisotropic vector mass term. At leading order it is therefore largely a temporal-sector deformation and is null in the orientation-difference HEE coefficient.
- **Case II** with  $\mu_X = 0$  is the exceptional case in which the change is exactly proportional to  $W_0$ ; it becomes a global rescaling of  $\mu^2$ .
- **Case III-a** adds a positive scalar cost  $U_\Phi$  to the vector operator. It can move the critical point, but because the scalar background is isotropic it cancels in  $S_\perp - S_\parallel$  at leading order.
- **Case III-b** modifies  $P$  and  $W_0$  through the single colour-blind radial factor  $Z_{\text{dm}}(\Phi(u))$  of the hidden dark-scalar kinetic portal. Its effect is therefore non-universal and must be computed from the full radial source.

Thus the hidden-SU(2) law below should be read as one solvable corner of a broader response classification, not as the organizing principle of the entire paper.

### 3.3 Minimal hidden SU(2) as a solvable benchmark

For the minimal hidden-SU(2) kinetic-mixing ensemble with no independent hidden chemical potential, the deformed equation reduces to (2.63). Defining

$$\hat{\mu}^2 \equiv \frac{\mu^2}{\tilde{\alpha}}, \quad \tilde{\alpha} = 1 - \frac{\alpha_{\text{dm}}^2}{4}, \quad (3.10)$$

turns the dark-deformed problem into the visible problem,

$$\partial_u(P\psi') + \hat{\mu}^2 W_0(u)\psi = 0. \quad (3.11)$$

The boundary conditions and eigenfunction are unchanged. Therefore  $\hat{\mu}_c = \mu_{c,\text{vis}}$  and

$$\frac{\mu_c(\alpha_{\text{dm}})}{\mu_c(0)} = \sqrt{1 - \frac{\alpha_{\text{dm}}^2}{4}}. \quad (3.12)$$

On the boundary side, this should not be oversimplified as a single scalar deformation  $S_{\text{CFT}} + \alpha_{\text{dm}} \int \mathcal{O}_{\text{hidden}}$ . The more faithful interpretation is a current-sector portal. Schematically, an effective description has

$$S_{\text{eff}} = S_{\text{HSV}}^{\text{vis}}[J] + S_{\text{HSV}}^{\text{hid}}[J_X] + \frac{\alpha_{\text{dm}}}{2} \int d^d x J_{\text{vis}}^{a\mu} J_{X\mu}^a + \dots, \quad (3.13)$$

This is only a schematic current-current mixing term; in the bulk variational problem the canonical momenta dual to  $J_{\text{vis}}$  and  $J_X$  are mixed. If the hidden source is set to zero, integrating out or eliminating the hidden channel induces an effective deformation of the visible current two-point function. In a UV-complete boundary theory such a portal may run under RG. In our bottom-up HSV description,  $\alpha_{\text{dm}}$  is treated as a fixed coupling of the finite-density scaling regime, while the holographic radial evolution computes the resulting scale dependence of the response. The special feature of Case II is that this flow collapses to the constant rescaling factor  $1 - \alpha_{\text{dm}}^2/4$ . This is precisely why it is a useful analytic benchmark.

Combining this with the baseline horizon scaling (3.6) gives

$$\frac{T_c(\alpha_{\text{dm}})}{T_c(0)} = \left(1 - \frac{\alpha_{\text{dm}}^2}{4}\right)^{-\frac{z}{2(n_h-2)}}. \quad (3.14)$$

This is why the hidden-SU(2) sector is useful: it supplies an analytic control curve against which the numerical figures can be read. It is not, by itself, a general theorem for all dark deformations. The proof works because the deformation is a constant rescaling of the electric weight and does not change the radial shape of the source-free zero mode.

### 3.4 How the exact rescaling is lost

The square-root law is lost whenever the dark sector introduces a new radial shape or a second boundary scale. The cleanest example is Case II with an independent hidden chemical potential. On the  $D = 4$  analytic reference sector  $(d, z, \theta) = (2, 1, 1/2)$  the reduced critical-point equation becomes

$$\frac{\mu_c^2 - (\alpha_{\text{dm}}^2/4)\mu_c\nu}{\tilde{\alpha}} = \frac{16}{3}, \quad (3.15)$$

where  $\nu \equiv \mu_X$  is the independent hidden chemical potential. The solution is

$$\mu_c(\alpha_{\text{dm}}, \nu) = \frac{1}{2} \left[ \frac{\alpha_{\text{dm}}^2}{4} \nu + \sqrt{\frac{\alpha_{\text{dm}}^4}{16} \nu^2 + \frac{64}{3} \tilde{\alpha}} \right]. \quad (3.16)$$

At  $\nu = 0$  this collapses to Eq. (3.12); at  $\nu \neq 0$  the additional term cannot be absorbed into  $\hat{\mu}$ . The scalar and tensor portals break the exact law for a different reason: they change the radial operator itself. In the language of Eq. (3.9), Case III-a contributes a positive  $U_\Phi$ , while Case III-b produces  $u$ -dependent changes in  $\delta P$ ,  $\delta W$ , and  $U_\Phi/Z_1$ .

This is the conceptual distinction used in the final figure set. Case II is shown with explicit  $\alpha_{\text{dm}}$  rescaling factors because its effect is analytic. The other cases are shown through their dark-minus-visible radial sources, critical values and HEE shifts because their response is not captured by a one-parameter scaling law.

## 4 RT surfaces, HEE response, and the condensate

The previous sections define the visible and dark-deformed radial equations and the critical scale  $\mu_c$ . This section explains the ordered-phase observables used in the figures. Its purpose is not to build a separate full phase diagram, but to make clear why HEE is a useful geometric probe, how the boundary regions are chosen, how the dark-sector radial source enters the RT variation, how the entanglement first-law check is normalised, and how the condensate  $\langle O \rangle$  is extracted from the nonlinear branch.

### 4.1 RT observables: interval, strip, slab, and orientation anisotropy

The visible ordered phase is anisotropic because the bulk field contains  $B_{x_1}^1 = \omega(u)$ . A critical chemical potential detects when this vector mode becomes normalizable, but it does not by itself measure how strongly the ordered state distinguishes the direction parallel to the condensate from transverse directions. HEE is sensitive to that distinction because the boundary entangling region can be oriented with respect to the vector order.

In  $D = 3$  the boundary has one spatial direction, and the entangling region is a line segment of length  $\ell$ . We write

$$\Delta S_{\text{int}} = \delta^2 \epsilon^2 \Delta S_{\text{int}}^{(2)} + O(\epsilon^4). \quad (4.1)$$

For  $D = 4, 5$  the region is a strip or slab: one direction has finite width  $W$ , while the remaining spectator directions are regulated by a transverse volume. If those spectator directions are compactified, the same construction may be viewed as a cylinder-like RT surface. The physical datum is the orientation of the finite-width direction. We compare a strip parallel to the condensate with a strip transverse to it and define

$$\mathcal{O}_{12}^{\text{EE}} = S_\perp - S_\parallel = \delta^2 \epsilon^2 \mathcal{O}_{12}^{(2)} + O(\epsilon^4). \quad (4.2)$$

This is the signed observable used in the corrected  $D = 4, 5$  figures. It is not a ratio.

The metric and dilaton are expanded as

$$g_{MN} = g_{MN}^{(0)} + \delta^2 \epsilon^2 g_{MN}^{(2)} + O(\epsilon^4), \quad \phi = \phi_0 + \delta^2 \epsilon^2 \phi_2 + O(\epsilon^4). \quad (4.3)$$

The first variation of the RT area functional on the undeformed surface  $\Sigma_0$  is

$$\delta S_{\text{RT}} = \frac{1}{8G_D} \int_{\Sigma_0} d^{D-2} \sigma \sqrt{\gamma^{(0)}} \gamma_{(0)}^{ab} g_{MN}^{(2)} \partial_a X^M \partial_b X^N. \quad (4.4)$$

Thus the calculation follows the chain

$$\omega_1, b_0 \longrightarrow T_{MN}^{(2)} \longrightarrow g_{MN}^{(2)} \longrightarrow \delta S_{\text{RT}}^{(2)}. \quad (4.5)$$

For  $D = 4, 5$  the traceless orientation response is encoded in a metric function  $A_2(u)$ , which satisfies

$$\left[ u^{d\theta+z+d+1} N_0(u) A_2'(u) \right]' = k_D S_{\text{aniso}}(u), \quad k_4 = -\frac{1}{4}, \quad k_5 = \frac{1}{3}, \quad (4.6)$$

with

$$S_{\text{aniso}}(u) = u^{d\theta+d+3z-3} N_0(u) w_1'(u)^2 - u^{d\theta+z+d-5} \frac{b_0(u)^2 w_1(u)^2}{N_0(u)}. \quad (4.7)$$

This is the anisotropic source shown in the radial-difference figures.

The constants  $k_4$  and  $k_5$  fix the normalization of the metric function  $A_2$ . We determine them by matching the numerical response to the closed visible solutions at the two analytic reference backgrounds. This convention reproduces the visible  $D = 4$  and  $D = 5$  metric profiles used in the RT calculation. A redefinition of  $A_2$  changes the source coefficient and the RT insertion together; the tensor-portal susceptibility below is a dark-to-visible ratio within one fixed dimension, so this common normalization cancels. We therefore do not interpret the absolute sign or normalization of  $k_D$  as an additional cross-dimensional result.

We can also check the first law to fix the normalization of the leading RT response. For a small interval, strip, or slab region  $\mathcal{A}$ , the relevant relation is the standard small-subregion entanglement first law,

$$\Delta E_{\mathcal{A}} = T_{\text{ent}} \Delta S_{\mathcal{A}}. \quad (4.8)$$

Here  $\Delta E_{\mathcal{A}}$  is obtained by integrating the homogeneous energy density over the same boundary region, including the regulated transverse volume for strip and slab regions. In the controlled  $z = 1$  normalization used for the first-law check, that energy density is read from the normalizable mass coefficient of the metric response; no additional thermodynamic parameter is introduced in the figure analysis.

For homogeneous small subregions the entanglement temperature scales as  $T_{\text{ent}} \sim 1/\ell$ . The appendix plots therefore display the leading undeformed entropy, its leading small-subregion variation, the dimensionless product  $T_{\text{ent}} \ell$ , and the difference between the two sides of Eq. (4.8). These plots are kept in the appendix because they validate the RT normalization rather than introducing a separate dark-sector mechanism. Extending this thermodynamic interpretation to generic HSV/Lifshitz exponents would require the full holographic stress tensor and counterterm scheme.

## 4.2 Dark-sector source rules and null channels

The orientation observable removes isotropic shifts. The two strip entropies are decomposed as

$$S_{\parallel} = S_{\text{iso}}^{(0)} - \frac{1}{2} \delta^2 \epsilon^2 \mathcal{O}_{12}^{(2)} + O(\epsilon^4), \quad S_{\perp} = S_{\text{iso}}^{(0)} + \frac{1}{2} \delta^2 \epsilon^2 \mathcal{O}_{12}^{(2)} + O(\epsilon^4). \quad (4.9)$$

The leading term is the undeformed HSV strip entropy. For a strip with turning point  $u_*$ , with  $p = 2d(1 + \theta)$  and  $q = d(1 + \theta) - 1$ , the finite part is

$$S_{\text{iso}}^{(0)} = 2 \left[ \int_{u_*}^{\infty} du \left( \frac{u^{q-1}}{\sqrt{N_0(u)} \sqrt{1 - (u_*/u)^p}} - u^{q-1} \right) - \frac{u_*^q}{q} \right], \quad (4.10)$$

with the usual logarithmic replacement for  $q = 0$ .

Equation (4.9) explains why Case I and Case III-a are null in  $\mathcal{O}_{12}^{(2)}$ : they are isotropic in the leading orientation channel and hence shift  $S_{\parallel}$  and  $S_{\perp}$  equally. Case II with  $\mu_X = 0$  rescales the same anisotropic source. In  $D = 3$  this gives

$$\Delta S_{\text{int}}^{(2)}(\alpha_{\text{dm}}) = \left( 1 - \frac{\alpha_{\text{dm}}^2}{4} \right) \Delta S_{\text{int}}^{(2)}(0), \quad (4.11)$$

and in  $D = 4, 5$  it gives

$$\mathcal{O}_{12}^{(2)}(\alpha_{\text{dm}}) = \left( 1 - \frac{\alpha_{\text{dm}}^2}{4} \right) \mathcal{O}_{12}^{(2)}(0). \quad (4.12)$$

Case III-b is not a constant-rescaling case: the scalar-dependent kinetic factor changes the radial weights of the anisotropic source, so the HEE response must be computed as a radial-shape effect.

### 4.3 Tensor-portal susceptibility as a linear response coefficient

We consider the quantity of susceptibility in the standard linear-response sense: it is the derivative of an observable with respect to the strength of an external deformation, evaluated at zero deformation. It is not assumed to be a pre-existing material constant. In the present bottom-up model the external deformation is the strength of the hidden dark-scalar kinetic portal. For the representative prescribed profile  $\Phi(u) = \Phi_h u^{-2}$ , the effective portal strength is

$$\lambda_{\text{TP}} = \alpha_{\text{dm}}^2 \beta \Phi_h^2. \quad (4.13)$$

For the strip-difference observable in  $D = 4, 5$ , we define

$$\chi_{\text{TP}}^{\text{strip}}(W) = \frac{\partial}{\partial \lambda_{\text{TP}}} \left[ \frac{\mathcal{O}_{12}^{(2)}(W; \lambda_{\text{TP}})}{\mathcal{O}_{12}^{(2)}(W; 0)} - 1 \right] \Bigg|_{\lambda_{\text{TP}}=0}. \quad (4.14)$$

The derivative is taken after recomputing both the normal-branch temporal profile and the vector zero mode with the same portal factor  $Z_{\text{dm}}$ . Thus  $\chi_{\text{TP}}^{\text{strip}}$  does not measure the explicit source multiplier alone. It measures the net change of the strip anisotropy after the dark portal reshapes  $b_0$ , reshapes  $\omega_1$ , and changes the traceless Yang–Mills source. A constant hidden-current rescaling gives no such width-dependent coefficient, and an isotropic dark source gives zero in the strip difference. This is the theoretical reason why the susceptibility is the natural observable for the tensor portal, while the exact Case-II scaling law remains only a benchmark.

The same construction could be applied to the  $D = 3$  interval coefficient, but that quantity is not the same strip-difference observable. We therefore reserve the notation  $\chi_{\text{TP}}^{\text{strip}}$  for the  $D = 4, 5$  strip comparison and report the interval response separately.

#### 4.4 Nonlinear condensate and extraction of $\langle O \rangle$

The order-parameter figures use  $\langle O \rangle$ , where

$$O \equiv J_{x_1}^1. \quad (4.15)$$

This is the boundary vector-current component dual to the normalizable part of the visible spatial gauge field  $B_{x_1}^1$ . It is not the dark scalar  $\Phi$ . A nonzero  $\langle O \rangle$  means that the visible  $SU(2)$  current has condensed along  $x_1$ , breaking spatial rotations.

The expectation value is extracted from the finite-amplitude source-free branch. We write

$$B = \varphi(u)\tau^3 dt + w(u)\tau^1 dx_1, \quad (4.16)$$

where  $\varphi$  is the temporal profile and  $w$  is the nonlinear vector profile. The probe equations are

$$(u^A N_0 w')' + \frac{u^r}{N_0} \varphi^2 w = 0, \quad (4.17)$$

$$(u^M \varphi')' - \frac{u^r}{N_0} \varphi w^2 = 0, \quad (4.18)$$

with

$$A = d\theta + d + 3z - 3, \quad M = d\theta + z + d - 1, \quad r = d(1 + \theta) + z - 5. \quad (4.19)$$

The horizon amplitude  $w(1) = w_{\text{hor}}$  is used as a continuation parameter to avoid the trivial solution  $w \equiv 0$ .

At the boundary,

$$\varphi(u) = \mu - \rho u^{-m} + \dots, \quad m = n_h - 2, \quad (4.20)$$

$$w(u) = w_{\text{src}} + w_{\text{vev}} u^{-\Delta_O} + \dots, \quad \Delta_O = d\theta + d + 3z - 4. \quad (4.21)$$

The source-free condition is  $w_{\text{src}} = 0$ , and the normalizable coefficient gives

$$\langle O \rangle = \mathcal{N}_O w_{\text{vev}}. \quad (4.22)$$

The constant  $\mathcal{N}_O$  is conventional, so the figures emphasize the critical point, the scaling with  $\mu - \mu_c$ , and the visible/dark displacement rather than an absolute vertical normalization.

Near the critical point,

$$\mu = \mu_c + \mu_2 w_{\text{hor}}^2 + O(w_{\text{hor}}^4), \quad \langle O \rangle = \mathcal{C} w_{\text{hor}} + O(w_{\text{hor}}^3), \quad (4.23)$$

so  $\langle O \rangle \propto (\mu - \mu_c)^{1/2}$ . For the minimal hidden  $SU(2)$  family, the nonlinear vector equation inherits the same effective electric rescaling as the critical-point problem,

$$(u^A N_0 w')' + \frac{1}{1 - \alpha_{\text{dm}}^2/4} \frac{u^r}{N_0} \varphi^2 w = 0, \quad (4.24)$$

so the condensate branch turns on at

$$\mu_c(\alpha_{\text{dm}}) = \mu_c(0) \sqrt{1 - \frac{\alpha_{\text{dm}}^2}{4}}. \quad (4.25)$$

Scalar and tensor portals are not inferred from this curve; they require their own finite-amplitude scalar–vector systems.

## 5 Dark-sector response beyond the visible baseline

The visible HSV solution already contains a nontrivial vector instability, radial profiles, condensate branch, and strip-entanglement anisotropy. The question in this section is therefore what remains after dark-sector deformations are compared against that visible baseline. Apart from the analytic hidden- $SU(2)$  rescaling law and the isotropic-channel selection rules, the dark-deformed zero-mode equations, the order- $\epsilon^2$  Einstein response, and the corresponding RT first variations are obtained by numerical boundary-value integration over the HSV parameter space<sup>2</sup>. The answer is organized in four steps. First, the strip difference acts as a filter: isotropic dark channels are removed, while rigid hidden-current rescalings survive only as constant factors. Second, the hidden dark-scalar kinetic portal produces a genuine susceptibility because it changes the radial profiles entering the anisotropic source. Third, the same self-consistent portal changes the critical scale in a way that depends on the HSV background. Finally, the radial profiles and condensate curves show how the small net HEE signal arises from a controlled ordered branch.

### 5.1 Selection rule and rigid benchmark

For  $D = 4, 5$  we use  $\mathcal{O}_{12}^{(2)} = S_{\perp}^{(2)} - S_{\parallel}^{(2)}$ . This observable subtracts the part of the RT response that is the same for the two strip orientations. Case I and the dark-scalar mass portal are therefore null at leading order because they do not generate a traceless source. Case II survives, but only as a rigid rescaling of the visible anisotropic source. The tensor portal is qualitatively different: it survives because it changes the radial profiles and hence the shape of the source, not merely its overall normalization.

---

<sup>2</sup>Code: [https://github.com/jiseongchae17hepth/Dark\\_sector\\_deformations\\_of\\_anisotropic\\_holographic\\_superfluid\\_in\\_hyperscaling\\_violation\\_geometry](https://github.com/jiseongchae17hepth/Dark_sector_deformations_of_anisotropic_holographic_superfluid_in_hyperscaling_violation_geometry)

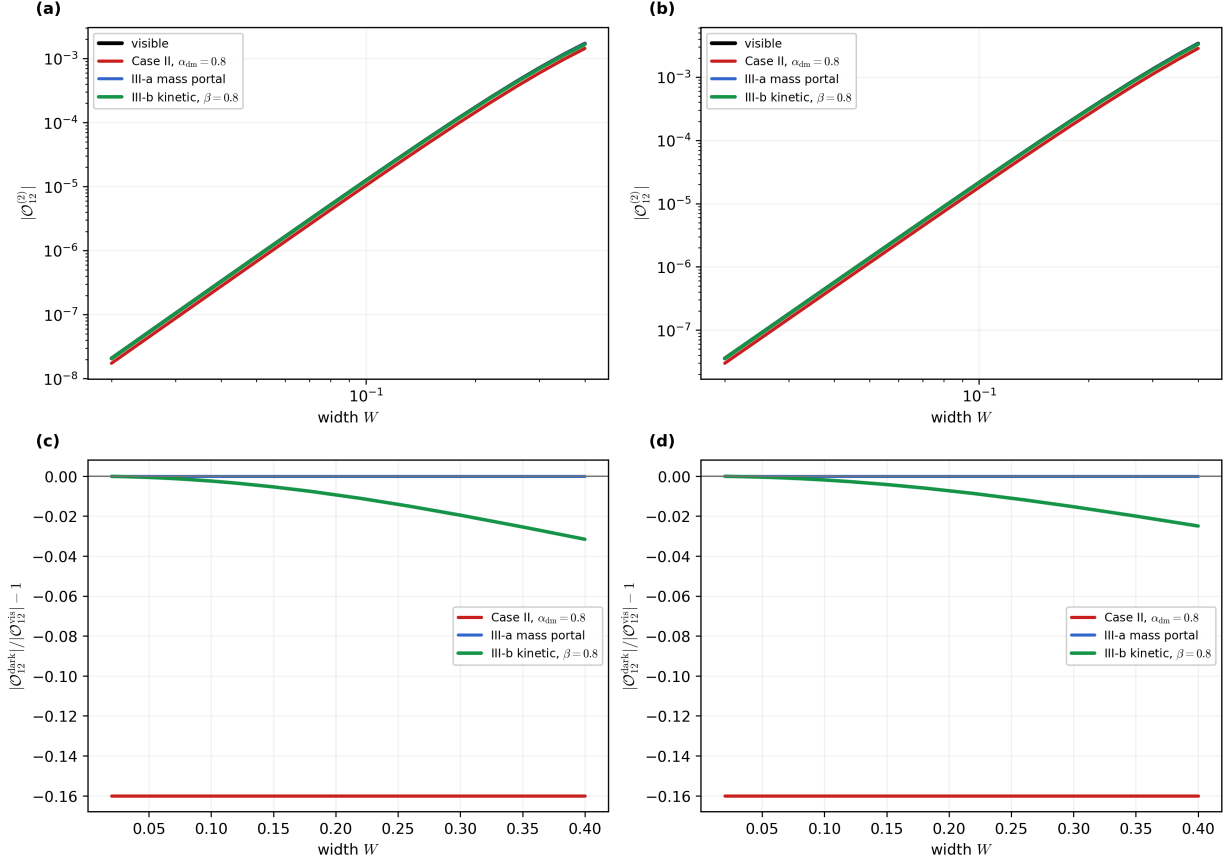


Figure 1: Strip-entanglement anisotropy in  $D = 4$  and  $D = 5$ . Panels (a) and (b) show  $|\mathcal{O}_{12}^{(2)}|$ ; panels (c) and (d) show the fractional change relative to the visible result. Case II gives the constant benchmark reduction, the isotropic mass portal lies on the visible curve, and the self-consistent kinetic portal with  $\beta = 0.8$ ,  $\Phi_h = 0.6$  gives a small width-dependent suppression. The same  $b_0^{(Z)}$  and  $\omega_Z$  profiles are used in the critical-point and HEE calculations.

This figure is the simplest visual statement of the selection rule. The null channels are not missing signals; they are removed by construction from the strip difference. The hidden-SU(2) curve is not a new radial effect; it is the constant rescaling predicted by the current-mixing benchmark. The only curve with nontrivial width dependence is the tensor portal. This motivates the susceptibility defined in Sec. 4.3.

## 5.2 Tensor-portal susceptibility and short-distance decoupling

We now evaluate  $\chi_{\text{TP}}^{\text{strip}}(W)$  from Eq. (4.14). For every value of the portal strength used in the finite-difference derivative, we solve Eq. (2.75) and the vector zero-mode equation (2.76), construct the resulting traceless source, and solve the metric-response boundary-value problem. The derivative is extracted from  $\beta = 0.01, 0.02, 0.04, 0.08$ . Over the displayed width range the largest finite-coupling change used in the fit is below 0.4%, so the susceptibility is not inferred from a large-response regime.

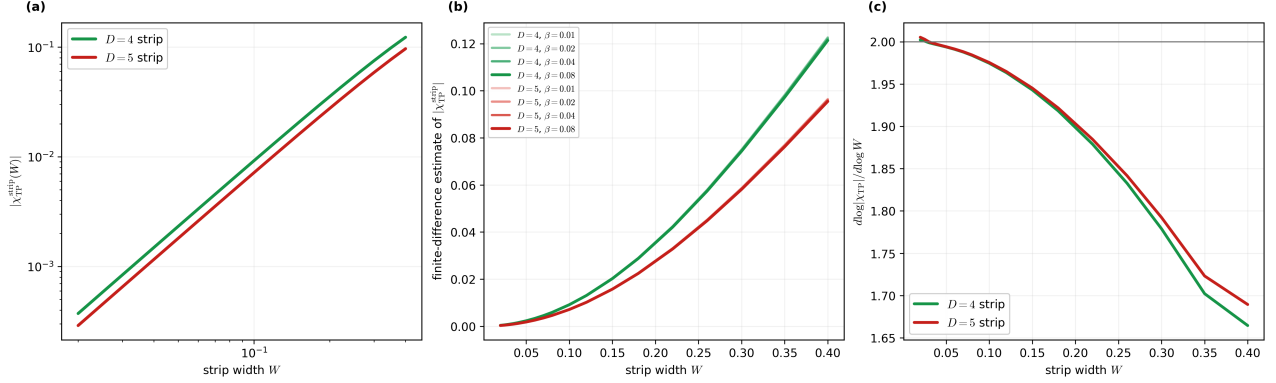


Figure 2: Self-consistent tensor-portal susceptibility for the  $D = 4$  and  $D = 5$  strips. Panel (a) shows the magnitude of the derivative in Eq. (4.14). The susceptibility itself is negative in both dimensions, so the kinetic portal suppresses the magnitude of the visible strip anisotropy. Panel (b) shows the finite-difference estimates obtained at the four small values of  $\beta$ ; their agreement verifies the derivative extraction. Panel (c) shows the local logarithmic slope of  $|\chi_{\text{TP}}^{\text{strip}}|$ . It approaches  $+2$  at short width, so the portal correction vanishes approximately as  $W^2$  rather than diverging.

The short-width behavior is the main physical lesson. The prescribed dark scalar is normalizable, so  $\Phi(u)$  vanishes near the asymptotic boundary. A sufficiently short strip therefore recovers the visible result: the tensor-portal susceptibility tends to zero, with  $|\chi_{\text{TP}}^{\text{strip}}| \propto W^2$  over the smallest widths resolved here. As the strip width increases, the RT surface samples deeper radial regions where the normalizable dark-scalar profile is larger, and the susceptibility grows smoothly. This is the cleanest UV/IR statement in the paper: the dark portal decouples from sufficiently short-distance entanglement but remains visible at larger strip width.

The negative sign is also informative. A source-only treatment would predict a much larger apparent enhancement. Once  $b_0$  and  $\omega_1$  are recomputed with the same  $Z_{\text{dm}}$ , the explicit source reweighting is partly cancelled by the profile changes. The net result at the two reference strip backgrounds is a small suppression of the visible anisotropy.

### 5.3 Critical scale and HSV-dependent sign change

The critical-scale scan is a supporting result, but it carries an independent message. Hidden-current mixing is a constant benchmark: in the minimal Case-II ensemble it lowers the visible critical scale by the exact square-root factor. The dark-scalar kinetic portal does not obey a universal sign rule. It changes the temporal profile, the vector zero mode, and the electric overlap simultaneously, so the sign of the shift is selected by the full HSV radial problem.

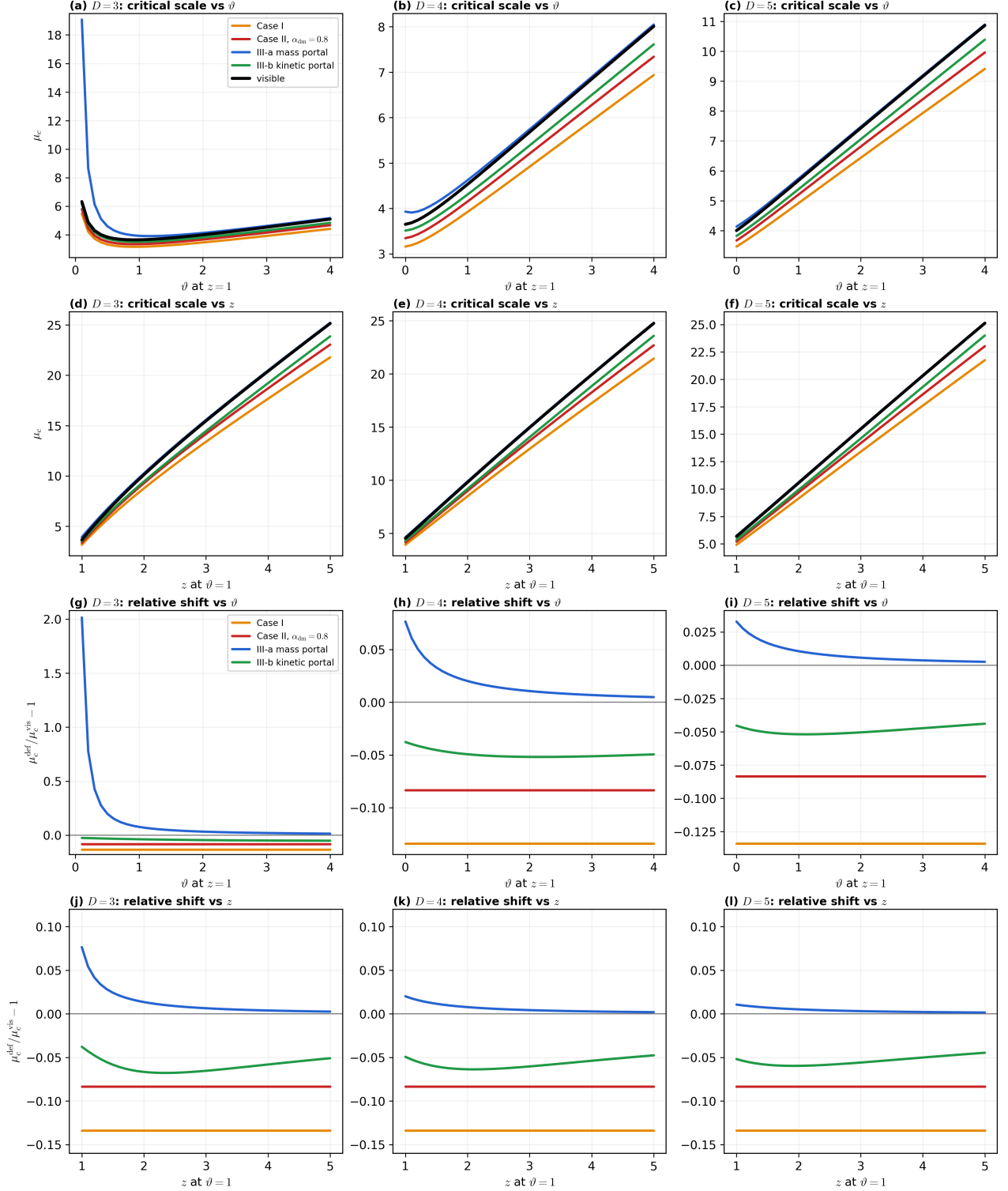


Figure 3: Critical scale across  $D = 3, 4, 5$ . Columns correspond to the three bulk dimensions. The first two rows show the solver boundary amplitude  $b_{\infty,c} = \sqrt{3}\mu_c$  as a function of  $\vartheta$  at  $z = 1$  and as a function of  $z$  at  $\vartheta = 1$ ; the last two rows show the corresponding fractional shift, which is the same for  $b_{\infty,c}$  and  $\mu_c$ . Case I is omitted because it coincides with the visible curve. Case II uses  $\alpha_{\text{dm}} = 0.8$ . The tensor portal uses  $\alpha_{\text{dm}} = 1$ ,  $\Phi_h = 0.6$ ,  $\Delta_\Phi = 2$ , and  $\beta = 0.8$ , with both  $b_0$  and  $\omega_1$  recomputed. It raises the critical scale at the three analytic reference backgrounds, but the sign changes in parts of the wider HSV scan.

This sign change is a useful diagnostic of the HSV dependence. A positive kinetic prefactor is not automatically superconductivity-enhancing or superconductivity-suppressing. The portal reshapes the radial kinetic term and the temporal electric profile at the same order, and the competition between these effects depends on  $(\vartheta, z)$ . This is why the critical scale is kept in the main text even though it is not the primary observable.

## 5.4 Self-consistent radial profiles and cancellation mechanism

The bulk profiles explain why the final susceptibility is small. Case II changes the critical amplitude but retains the visible zero-mode shape. The kinetic portal changes the temporal profile, the vector zero mode, and the anisotropic source at the same time. The visible and dark radial fields can therefore look close in  $\omega_1$  while producing a nontrivial dark-minus-visible traceless source.

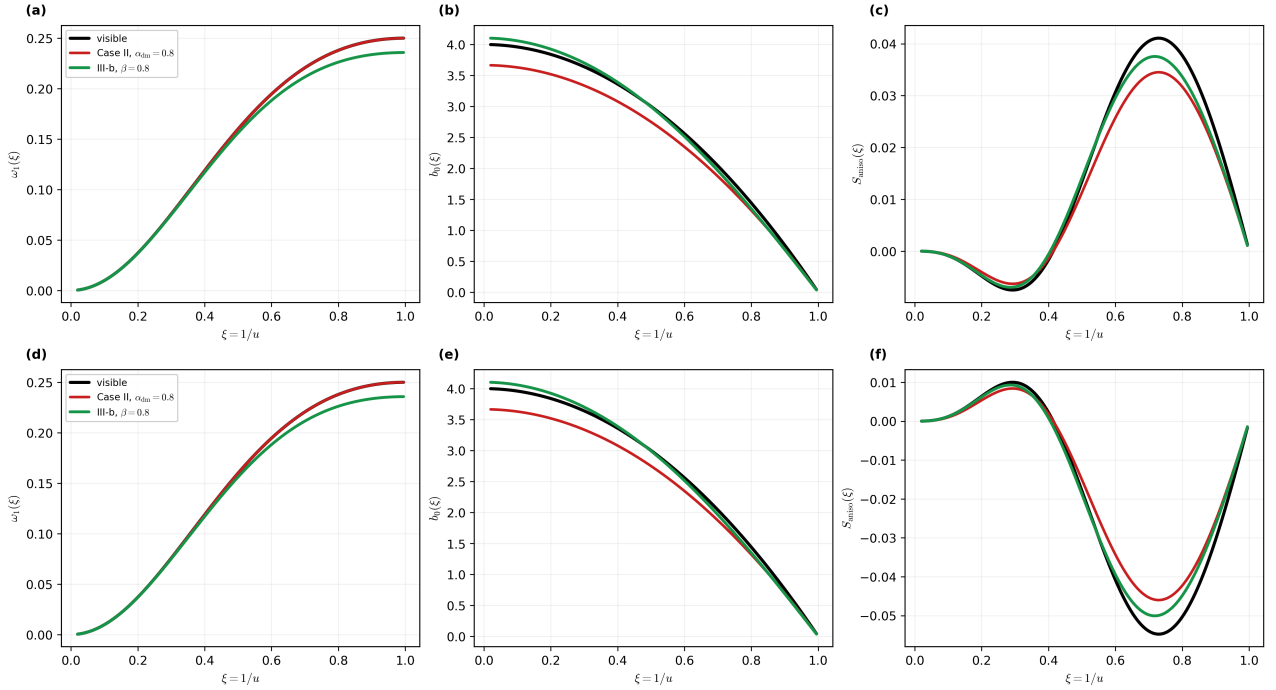


Figure 4: Self-consistent radial data at the  $D = 4$  reference background (top row) and the  $D = 5$  reference background (bottom row). From left to right the panels show  $\omega_1(\xi)$ ,  $b_0(\xi)$ , and  $S_{\text{aniso}}(\xi)$ . The visible solution is compared with the Case-II benchmark and the kinetic portal at  $\beta = 0.8$ ,  $\Phi_h = 0.6$ . The kinetic portal does not act as a simple multiplicative weight: both radial fields move before the source is evaluated.

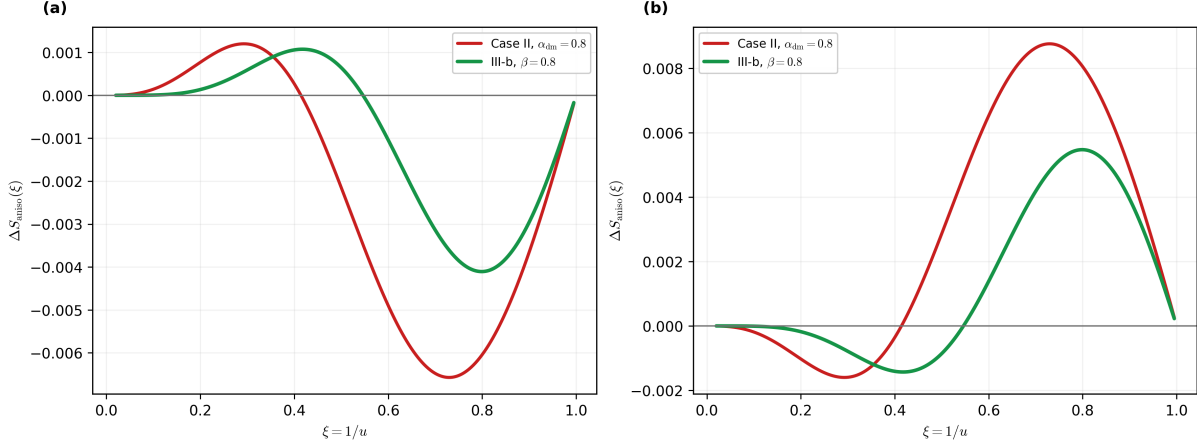


Figure 5: Dark-minus-visible traceless source in  $D = 4$  and  $D = 5$ . The Case-II curve is the rigid benchmark rescaling. The tensor-portal curve is the full difference  $S_{\text{aniso}}[b_0^{(Z)}, \omega_Z, Z] - S_{\text{aniso}}[b_0, \omega, 1]$ , not the source-only approximation  $(Z - 1)S_{\text{aniso}}^{\text{vis}}$ . Its sign changes along the radial direction, which produces the partial cancellation seen in the strip susceptibility.

The radial source changes appreciably even though the final short-strip susceptibility is small. The RT integral averages positive and negative parts of this source together with the induced metric response. This cancellation is why the self-consistent calculation gives short-width decoupling rather than the artificial enhancement produced by a source-only reweighting.

## 5.5 Condensate branches below the critical point

The linear analysis of the critical scale and entanglement response locates instabilities and classifies their geometric response, but a linear zero mode by itself does not prove that an ordered phase actually forms. The condensate curves close this gap for the visible branch and the analytically controlled hidden-current benchmark. Solving the full nonlinear vector equation below  $T_c$  produces a source-free branch on which  $\langle O \rangle \equiv \langle J_{x_1}^1 \rangle$  grows continuously from zero with the mean-field square-root behavior expected of a second-order transition. Turning on Case II mixing displaces the whole branch to lower visible chemical potential by the same square-root factor that controls the critical point and the HEE rescaling.

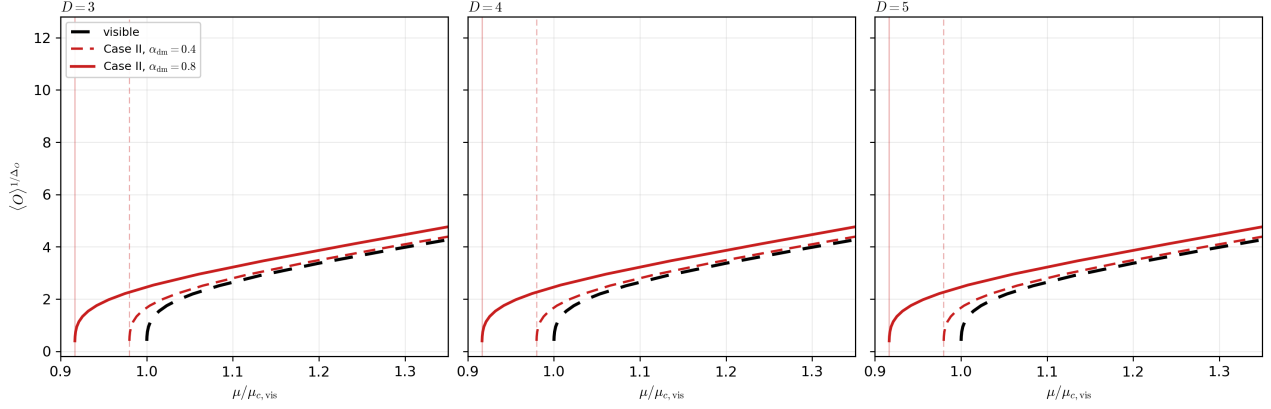


Figure 6: Nonlinear condensate  $\langle O \rangle^{1/\Delta_O}$  versus  $\mu/\mu_{c,\text{vis}}$  in  $D = 3, 4, 5$ . Each panel compares the visible branch with Case II hidden-current mixing at  $\alpha_{\text{dm}} = 0.4$  and  $0.8$ . The vertical guide lines mark the corresponding critical shifts  $\sqrt{1 - \alpha_{\text{dm}}^2/4}$ , while the curves show that the source-free ordered branch follows the same displacement predicted by the linear analysis.

These curves are used as consistency checks, not as a full nonlinear dark-scalar phase diagram. They show that the visible zero mode and the solvable hidden-current benchmark connect to ordered source-free branches. Extending the same nonlinear analysis to the self-consistent dark scalar portal would require solving the scalar sector dynamically, which is beyond the probe calculation used here. The remaining appendix figures are normalization and benchmark checks rather than separate claims. The Case-II  $\vartheta$ - and  $z$ -overlays appear in Figs. 9 and 10, and the first-law normalization checks appear in Figs. 11, 12, and 13.

## 6 Discussion

### 6.1 Boundary interpretation of the dark deformations

The safest interpretation of our results is as a set of controlled current-sector deformations of an effective HSV boundary regime. The visible Abelian background fixes a finite-density state. The visible non-Abelian bulk field is dual to a flavor-current multiplet  $J_\mu^a$ , and the ordered branch is the vector-current condensate

$$\langle O \rangle \equiv \langle J_{x_1}^1 \rangle. \quad (6.1)$$

Thus the central question is not whether an abstract dark field changes a black-brane solution, but which boundary current channel it deforms and how that deformation is projected onto observable quantities.

For the hidden-gauge cases, the boundary deformation is naturally current-current rather than single-operator scalar. A schematic effective description is

$$S_{\text{bdy}} = S_{\text{HSV}}^{\text{vis}}[J] + S_{\text{HSV}}^{\text{hid}}[J_X] + \frac{\alpha_{\text{dm}}}{2} \int d^d x J_{\text{vis}}^{a\mu} J_{X\mu}^a + \dots \quad (6.2)$$

This expression is not meant as a microscopic Lagrangian for the unknown HSV field theory; it only indicates an off-diagonal source/response matrix between visible and hidden conserved currents. In

the bulk this off-diagonal structure is exactly the kinetic mixing of gauge fields. When the hidden source is held fixed or set to zero, the hidden current sector can be eliminated, leaving an induced deformation of the visible current susceptibility. This is the origin of the factor  $1 - \alpha_{\text{dm}}^2/4$  in the minimal Case-II ensemble.

From an RG perspective,  $\alpha_{\text{dm}}$  is a portal coupling of the effective current sector. If the HSV regime is embedded in a UV-complete theory, this coupling may have a beta function and can trigger a flow of the current two-point matrix. We do not compute that UV beta function. Instead, the holographic calculation treats  $\alpha_{\text{dm}}$  as a parameter of the finite-density scaling regime and computes the radial flow of response functions within that regime. In Case II this radial flow is trivial in the sense that the dark response remains a constant rescaling factor. In Case III-b the scalar-dependent kinetic factor  $Z_{\text{dm}}(\Phi(u))$  makes the deformation genuinely radial and therefore profile-dependent.

Cases III-a and III-b have a different boundary interpretation from hidden-gauge kinetic mixing, but they are still dark-sector deformations. They introduce an independent dark scalar operator  $\mathcal{O}_\Phi$ , neutral only with respect to the visible  $SU(2)$  flavor symmetry, and couple it to the visible current sector through  $\alpha_{\text{dm}}$ -controlled portal terms. Case III-a is an isotropic dark-scalar mass portal for the visible vector mode. Case III-b is a dark-scalar kinetic portal that makes the effective Yang–Mills kinetic operator depend on  $\Phi(u)$ . Boundary-wise, the scalar cases describe a dark scalar environment that can imitate, suppress, or enhance the visible vector-current instability without introducing a second hidden gauge current.

This distinction explains why different observables see different parts of the same dark deformation. The critical scale  $\mu_c$  probes the lowest eigenvalue of the vector-current zero-mode operator. The radial source plots probe the bulk distribution of stress produced by that zero mode. The HEE coefficient probes how the corresponding order- $\epsilon^2$  metric response is integrated by an interval, strip, or slab RT surface. The condensate plots probe the finite-amplitude source-free branch. Since these are different projections of the current-sector deformation, it is not expected that a case which is visible in  $\mu_c$  must be equally dramatic in  $\mathcal{O}_{12}^{(2)}$ , or conversely.

## 6.2 What HSV adds beyond the asymptotically AdS superfluid

The HSV geometry should not be read as the UV completion of a known microscopic Lagrangian. It is an effective scaling regime of a finite-density boundary theory with dynamical exponent  $z$  and hyperscaling-violation exponent  $\vartheta$ . The role of the bulk computation is therefore to ask how a visible vector-current instability and its hidden-current deformations behave when the radial weights are those of a nonrelativistic, hyperscaling-violating regime rather than those of asymptotically AdS. This is precisely the regime where a simple AdS result can either survive as a universal rescaling factor or become a profile-dependent response.

The hidden- $SU(2)$  law is the case in which the rescaling survives. The reduced critical operator contains  $\alpha_{\text{dm}}$  only through  $\tilde{\alpha} = 1 - \alpha_{\text{dm}}^2/4$ , so

$$\frac{\mu_c(\alpha_{\text{dm}})}{\mu_c(0)} = \sqrt{1 - \frac{\alpha_{\text{dm}}^2}{4}}. \quad (6.3)$$

Because the radial eigenfunction class is unchanged, this relation persists across the scanned HSV parameters. That persistence is meaningful: it says that not every beyond-AdS deformation destroys the hidden-current rescaling factor. The tensor portal is the opposite case. It changes the radial weight of the visible current operator, so the response depends on where the RT kernel and the vector stress overlap in the HSV radial direction.

### 6.3 Physical reading of the result in different dimensions

The  $D = 3$  figures should be interpreted as interval probes of the total metric response. Since there is no independent transverse strip orientation, the interval coefficient  $\Delta S_{\text{int}}^{(2)}$  does not enforce the same isotropic-sector null rule as  $\mathcal{O}_{12}^{(2)}$  in higher dimensions. Thus a hidden charge-sector deformation can remain visible in  $D = 3$  even when its higher-dimensional strip-anisotropy counterpart is null. This makes  $D = 3$  a useful check of the full response chain, but not the sharpest check of directional anisotropy.

The  $D = 4$  and  $D = 5$  HEE figures are sharper because they use the signed orientation difference

$$\mathcal{O}_{12}^{(2)} = S_{\perp}^{(2)} - S_{\parallel}^{(2)}. \quad (6.4)$$

This observable is designed to subtract the isotropic part of the RT response. Therefore Case I and Case III-a are not expected to produce a leading signal unless they generate an anisotropic stress component. Their near-coincidence with the visible curve is not a numerical failure; it is a selection rule of the observable. Case II is visible because it rescales the vector stress. Case III-b is visible because it changes the radial kinetic matrix and therefore the source profile feeding the metric perturbation.

The condensate figures add a complementary statement. They verify that the zero-mode critical point corresponds to a source-free ordered branch and not merely to a linearized eigenvalue. In the Case-II curves, the hidden sector lowers the chemical potential needed to form  $\langle J_{x_1}^1 \rangle$ ; at fixed visible normalization this appears as a leftward displacement of the condensate curve. We use these curves to support the critical-point interpretation, not to claim a full global nonlinear phase diagram for every dark deformation.

### 6.4 Limitations and future works

The present form of the paper is deliberately conservative because several points are natural places for a referee to press. First, we do not claim to have identified the microscopic HSV boundary Lagrangian. HSV geometries are used as effective nonrelativistic finite-density scaling regimes. The physical statement is therefore about the response of the current sector within that regime, not about a unique UV-complete material.

Second, the four dark sectors do not have identical microscopic status. Cases I and II are hidden gauge sectors and have the usual kinetic-mixing interpretation. Cases III-a and III-b are hidden dark-scalar portal models. They are not visible scalar deformations:  $\Phi$  is independent of the visible  $SU(2)$  multiplet and couples to it only through  $\alpha_{\text{dm}}$ -controlled portals. The word “dark” is therefore used in a specific bottom-up sense: a field outside the visible  $p$ -wave order-parameter sector modifies the visible

current response through a portal. This keeps the title accurate while distinguishing hidden-gauge portals from hidden-scalar portals.

Third, the exact square-root law is not promoted to a universal theorem for all dark deformations. It is a solvable benchmark that follows from the constant rescaling of the electric weight in the minimal hidden- $SU(2)$  ensemble. The moment an independent hidden chemical potential or a radial scalar weight is introduced, the response becomes operator-dependent. This is why the figures compare Case II with the dark-scalar portals instead of using the square-root law as a global fitting template.

Fourth, the thermodynamic statements are kept at the level supported by the calculation. Probe free-energy data are not used as evidence for the tensor-portal result because the present probe calculation does not provide the fully renormalized grand potential. The HEE results use the order- $\epsilon^2$  metric response and small-subregion RT expansion. The first-law plots test the normalization of the RT response in the controlled scope described in Sec. 4. The nonlinear condensate curves show that the linear critical point is connected to a source-free ordered branch; they are not a full back-reacted global phase diagram.

Fifth, the kinetic-mixing parameter is restricted to the positive-kinetic regime  $1 - \alpha_{\text{dm}}^2/4 > 0$ . We do not explore the singular endpoint where the effective kinetic matrix degenerates. We also do not interpret the dark-scalar portal as a direct dark-matter particle model. It is a holographic portal deformation designed to separate isotropic scalar stress from anisotropic vector-current stress.

A natural way to increase the physical scope is to stop prescribing  $\Phi(u)$  and solve the hidden scalar sector dynamically. That extension is not a cosmetic change. One would need to specify a scalar potential  $V(\Phi)$ , impose either a dark scalar source or a normalizable boundary condition, solve the scalar equation together with the visible gauge fields, and include the scalar stress tensor in the Einstein equations. The portal factor  $Z_{\text{dm}}(\Phi)$  would then be determined by a genuine dark-sector saddle rather than by an externally chosen profile. The critical scale, strip susceptibility, condensate branch, and thermodynamic potential could all change because the dark scalar would reshape the geometry and the normal-branch electric field at the same time.

A fully back-reacted treatment would also be the right framework for thermodynamics. In the present probe calculation the condensate curves verify the existence of a source-free ordered branch, and the first-law plots check the RT normalization, but we do not compute the renormalized grand potential of the coupled visible–dark system. A dynamical scalar/back-reacted analysis would have to include the bulk gravitational action, the Gibbons–Hawking term, counterterms appropriate to the HSV asymptotics, and the scalar contribution to the boundary stress tensor. Only then could one ask whether the tensor portal changes the global phase diagram rather than only the linear response and the local ordered branch.

This is why the present result is phrased as a controlled susceptibility rather than as a dark-matter model or a complete phase diagram. The prescribed normalizable scalar profile is enough to separate three effects—the null selection rule of isotropic channels, the rigid rescaling of hidden-current mixing, and the short-distance decoupling of the kinetic portal. The larger-impact problem is to determine whether these features persist, strengthen, or disappear when the dark scalar is promoted to a dynamical field and allowed to backreact on the HSV geometry.

With these qualifications, the results separate into two tiers. The exactly soluble hidden-SU(2) rescaling and the null channels of the temporal  $U(1)$  and isotropic mass portal are useful benchmarks. The substantive result is the tensor-portal susceptibility extracted from the  $D = 4, 5$  strip-entanglement difference after both  $b_0$  and  $\omega_1$  are recomputed. It is negative at the two reference backgrounds, so the portal slightly suppresses the visible anisotropy, and its magnitude vanishes approximately as  $W^2$  toward short width. This behavior is consistent with the normalizable dark-scalar profile disappearing near the boundary. The  $D = 3$  interval is reported separately because it is not the same strip-difference observable. The broader point is that the strip difference distinguishes a radial dark portal from rigid current rescalings while remaining insensitive to it at sufficiently short distance.

## A Supplementary figures and consistency checks

The main text keeps the figures that carry the main physics: the tensor-portal susceptibility, the dimension-resolved critical-point comparison, the strip-entanglement response, the self-consistent radial profiles, and the nonlinear condensate check. The figures below are restricted to analytic examples and first-law normalization checks.

### A.1 Additional Case-II $\alpha_{\text{dm}}$ overlays

The two figures below record the closed Case-II benchmark used to normalize the rest of the calculation. They are not part of the main novelty, but they are useful for reproducing the analytic control case.

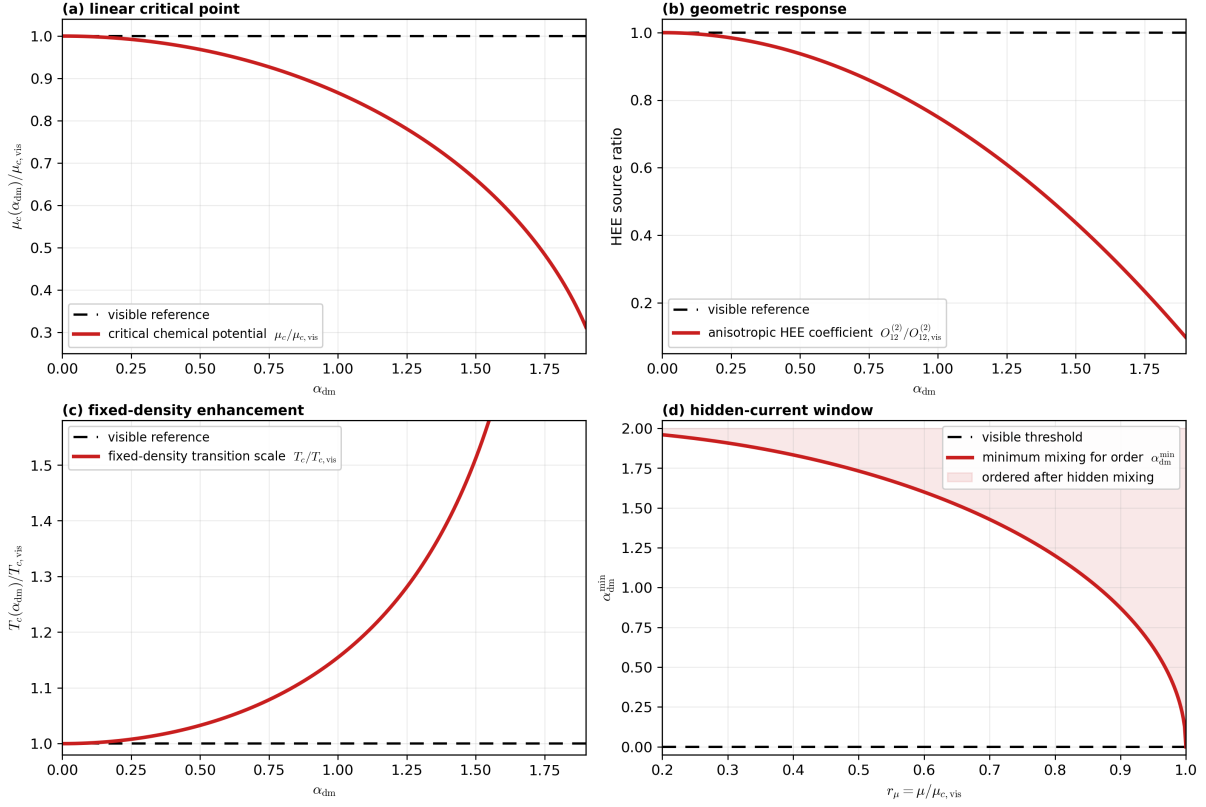


Figure 7: Case-II hidden- $SU(2)$  rescaling factors controlled by  $\alpha_{\text{dm}}$ . The critical chemical-potential factor and the order- $\epsilon^2$  HEE source factor follow from the same constant kinetic-mixing rescaling. The plot is kept as a benchmark rather than as the main result.

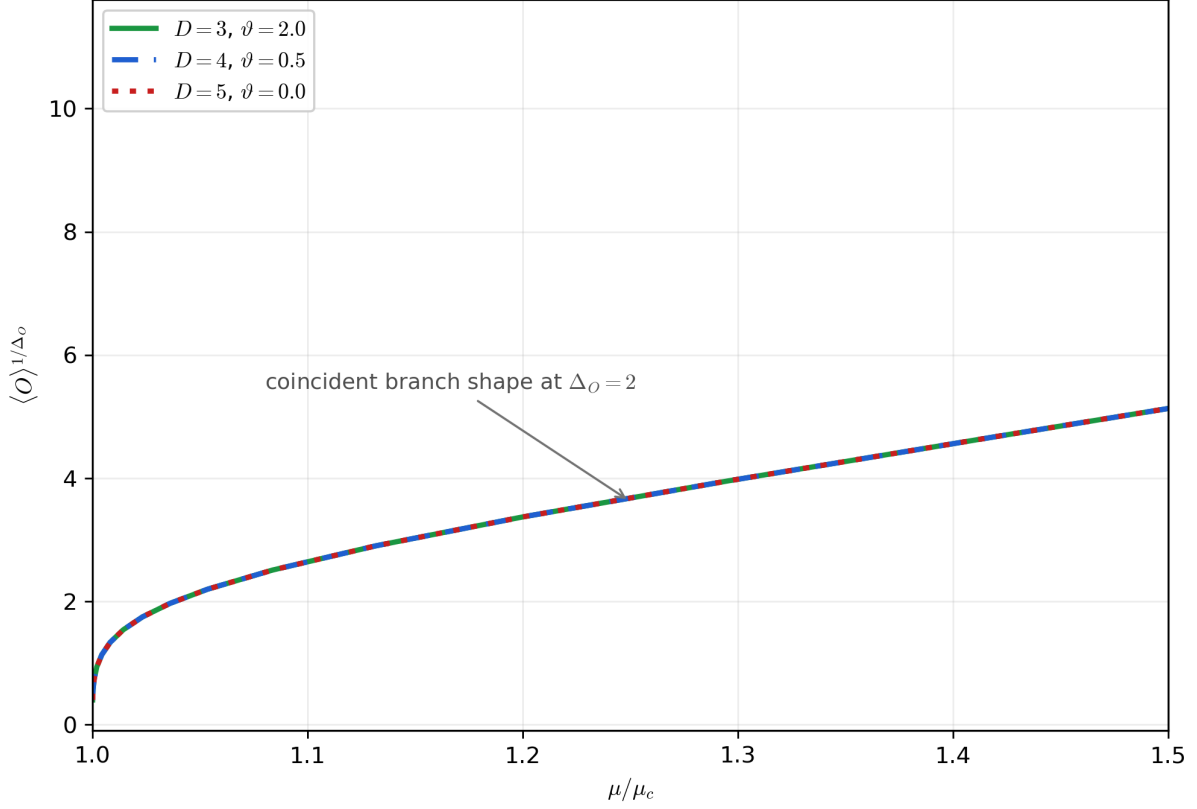


Figure 8: Case-II condensate curves at the analytic reference backgrounds in  $D = 3, 4, 5$ , with  $\alpha_{\text{dm}} = 0, 0.4, 0.8, 1.2$ . The curves verify that the nonlinear branch inherits the same benchmark critical displacement.

The two overlays below ask a narrower question: does the Case-II leftward critical shift remain visible when the HSV geometry is varied? The answer is yes. They are placed here because they confirm robustness of the same benchmark mechanism rather than adding a new one.

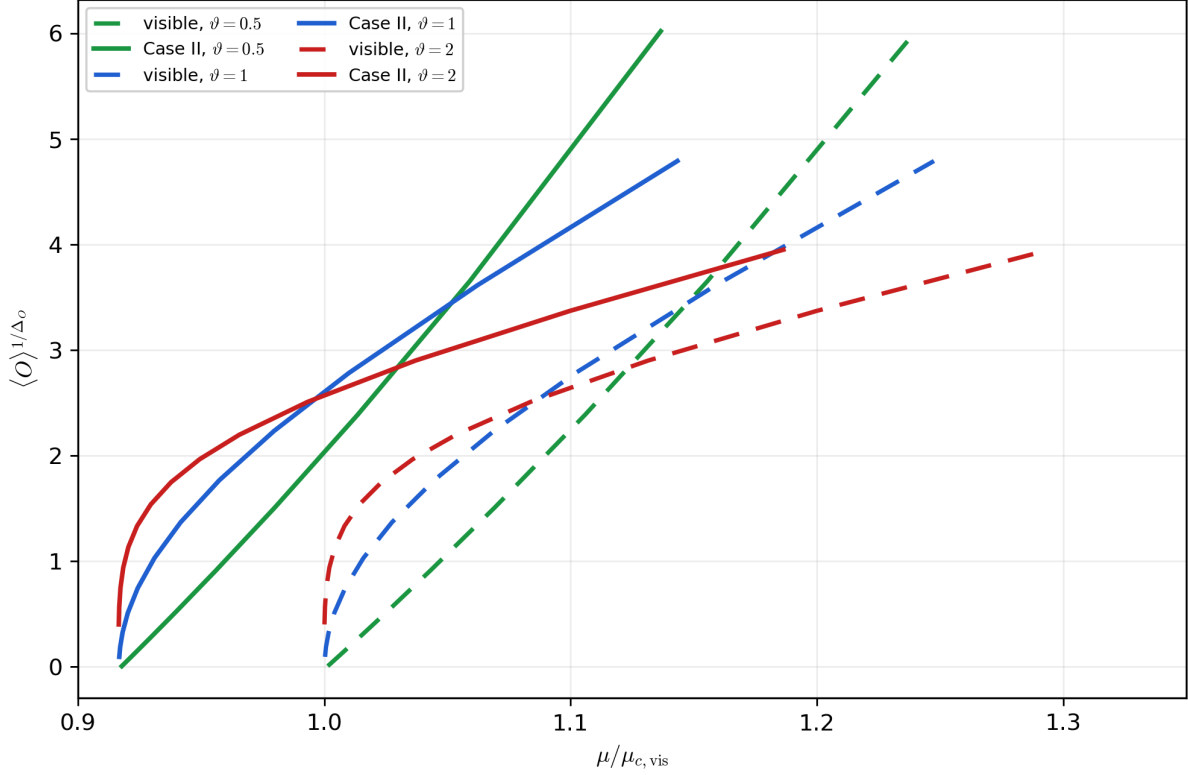


Figure 9: Case-II condensate overlay at fixed  $\alpha_{\text{dm}} = 0.8$  and  $z = 1$ , with visible curves dashed and dark curves solid. Each color corresponds to a different  $\vartheta$ . The hidden-sector curve associated with a given visible curve starts at lower  $\mu/\mu_{c,\text{vis}}$ , while the overall branch shape still reflects the visible HSV exponent.

Figure 9 separates two effects. The hyperscaling exponent changes the condensate scale and curvature, whereas  $\alpha_{\text{dm}}$  shifts the critical point. This is why the figure supports the main Case-II claim without needing to be part of the main figure set.

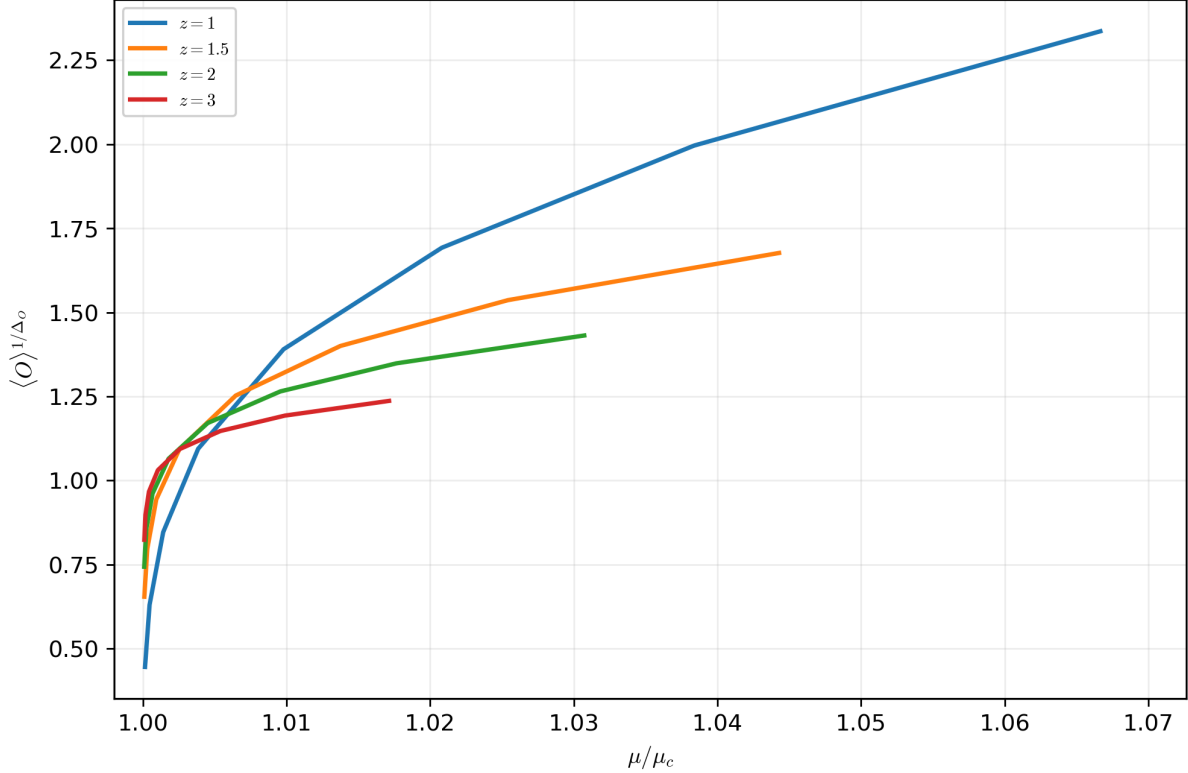


Figure 10: Case-II condensate overlay at fixed  $\alpha_{\text{dm}} = 0.8$  along representative  $z$ -slices of the controlled reference backgrounds. Visible curves are dashed and dark curves are solid. The plot shows that the universal hidden-sector shift and the residual  $z$ -dependence of the visible condensate can be disentangled.

Figure 10 plays the same role for the dynamical exponent. It demonstrates that varying  $z$  changes the branch shape, but does not remove the Case-II critical displacement. This is a robustness check for the rescaling factors in Fig. 7.

## A.2 Supporting figures in $D = 3$

The  $D = 3$  interval is a different observable from the  $D = 4, 5$  strip difference and is not used in the tensor-portal susceptibility. The first-law figure below is retained only as a normalization check.

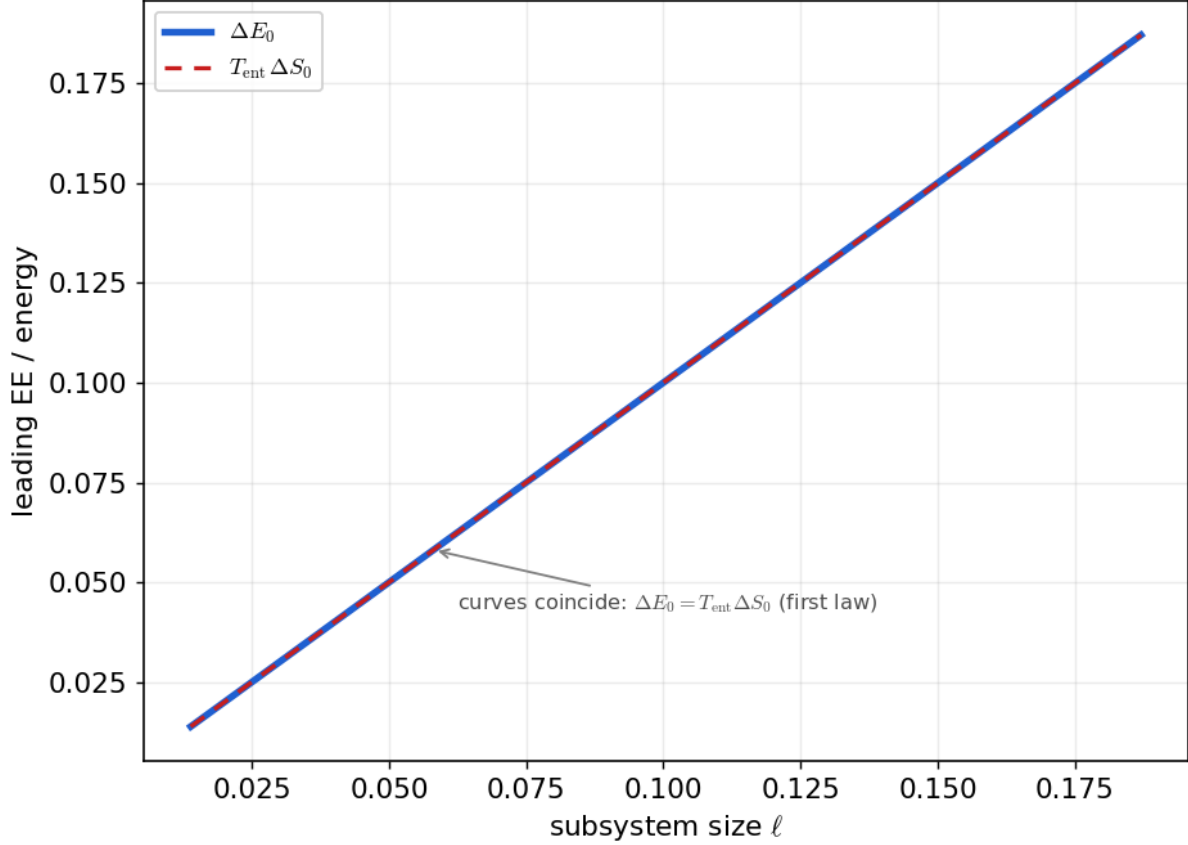


Figure 11: Leading strip entropy and first-law check in  $D = 3$ . It validates the RT normalization and is not a separate dark-sector effect.

### A.3 Supporting figures in $D = 4$

The  $D = 4$  main text contains the self-consistent strip response. The appendix retains only the first-law normalization check.

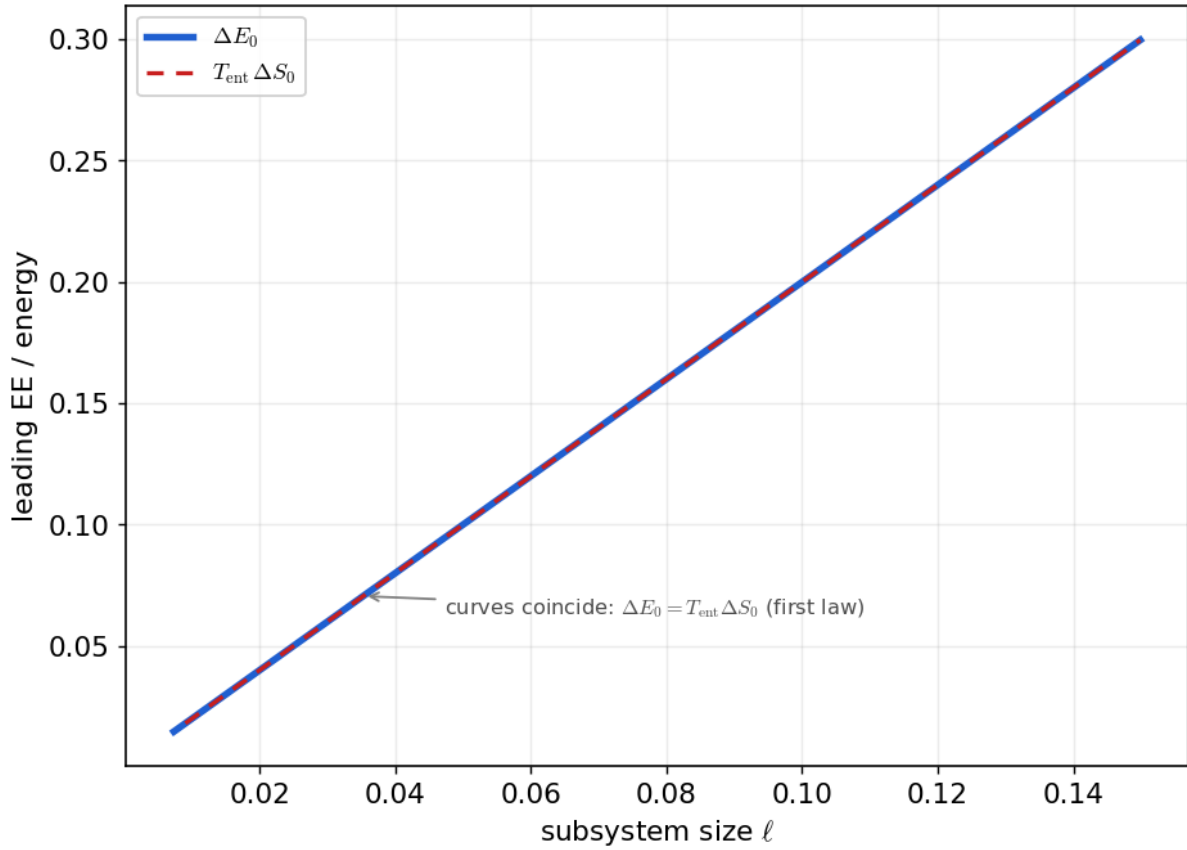


Figure 12: Leading strip entropy and first-law check in  $D = 4$ . The controlled interpretation is the  $z = 1$  small-subsystem relation. The figure checks the RT normalization used in the HEE analysis.

#### A.4 Supporting figures in $D = 5$

The  $D = 5$  main text contains the self-consistent strip response. The appendix retains only the first-law normalization check.

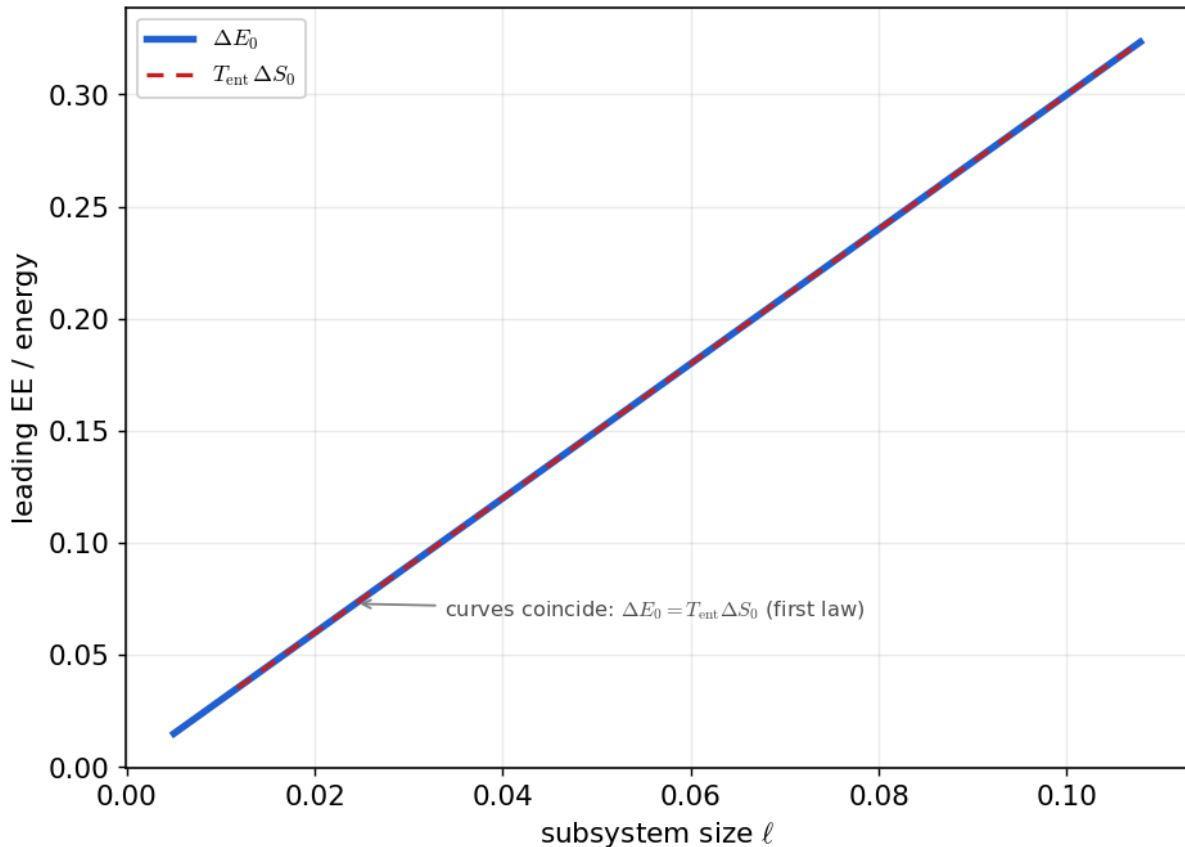


Figure 13: Leading strip entropy and first-law check in  $D = 5$ . The figure checks the small-subsystem RT normalization. It validates the calculation rather than adding a new dark-sector channel.

## References

- [1] J. M. Maldacena, “The Large N limit of superconformal field theories and supergravity,” *Adv. Theor. Math. Phys.* **2** (1998) 231 [hep-th/9711200].
- [2] S. S. Gubser, I. R. Klebanov and A. M. Polyakov, “Gauge theory correlators from non-critical string theory,” *Phys. Lett. B* **428** (1998) 105 [hep-th/9802109].
- [3] E. Witten, “Anti-de Sitter space and holography,” *Adv. Theor. Math. Phys.* **2** (1998) 253 [hep-th/9802150].
- [4] O. Aharony, S. S. Gubser, J. M. Maldacena, H. Ooguri and Y. Oz, “Large N field theories, string theory and gravity,” *Phys. Rept.* **323** (2000) 183 [hep-th/9905111].
- [5] D. T. Son and A. O. Starinets, “Minkowski-space correlators in AdS/CFT correspondence,” *JHEP* **09** (2002) 042 [hep-th/0205051].
- [6] N. Iqbal and H. Liu, “Universality of the hydrodynamic limit in AdS/CFT and the membrane paradigm,” *Phys. Rev. D* **79** (2009) 025023 [arXiv:0809.3808].

- [7] G. Policastro, D. T. Son and A. O. Starinets, “The shear viscosity of strongly coupled N=4 supersymmetric Yang–Mills plasma,” *Phys. Rev. Lett.* **87** (2001) 081601 [hep-th/0104066].
- [8] G. Policastro, D. T. Son and A. O. Starinets, “From AdS/CFT correspondence to hydrodynamics,” *JHEP* **09** (2002) 043 [hep-th/0205052].
- [9] P. Kovtun, D. T. Son and A. O. Starinets, “Viscosity in strongly interacting quantum field theories from black hole physics,” *Phys. Rev. Lett.* **94** (2005) 111601 [hep-th/0405231].
- [10] S. Bhattacharyya, V. E. Hubeny, S. Minwalla and M. Rangamani, “Nonlinear fluid dynamics from gravity,” *JHEP* **02** (2008) 045 [arXiv:0712.2456].
- [11] S. Bhattacharyya, R. Loganayagam, S. Minwalla, S. Nampuri, S. P. Trivedi and S. R. Wadia, “Forced fluid dynamics from gravity,” *JHEP* **02** (2009) 018 [arXiv:0806.0006].
- [12] S. S. Gubser and S. S. Pufu, “The gravity dual of a p-wave superconductor,” *JHEP* **11** (2008) 033 [arXiv:0805.2960].
- [13] M. M. Roberts and S. A. Hartnoll, “Pseudogap and time reversal breaking in a holographic superconductor,” *JHEP* **08** (2008) 035 [arXiv:0805.3898].
- [14] J. Erdmenger, P. Kerner and H. Zeller, “Non-universal shear viscosity from Einstein gravity,” *Phys. Lett. B* **699** (2011) 301 [arXiv:1011.5912].
- [15] P. Basu and J. H. Oh, “Analytic approaches to anisotropic holographic superfluids,” *JHEP* **07** (2012) 106 [arXiv:1109.4592].
- [16] J. H. Oh, “Running shear viscosities in anisotropic holographic superfluids,” *JHEP* **06** (2012) 103 [arXiv:1201.5605].
- [17] B. Holdom, “Two U(1)’s and epsilon charge shifts,” *Phys. Lett. B* **166** (1986) 196.
- [18] K. R. Dienes, C. F. Kolda and J. March-Russell, “Kinetic mixing and the supersymmetric gauge hierarchy,” *Nucl. Phys. B* **492** (1997) 104 [hep-ph/9610479].
- [19] S. A. Abel and B. W. Schofield, “Brane-antibrane kinetic mixing, millicharged particles and SUSY breaking,” *Nucl. Phys. B* **685** (2004) 150 [hep-th/0311051].
- [20] S. A. Abel, J. Jaeckel, V. V. Khoze and A. Ringwald, “Illuminating the hidden sector of string theory by shining light through a magnetic field,” *Phys. Lett. B* **666** (2008) 66 [hep-ph/0608248].
- [21] S. A. Abel, M. D. Goodsell, J. Jaeckel, V. V. Khoze and A. Ringwald, “Kinetic mixing of the photon with hidden U(1)s in string phenomenology,” *JHEP* **07** (2008) 124 [arXiv:0803.1449].
- [22] L. Nakoneczny and M. Rogatko, “Analytic study on backreacting holographic superconductors with dark matter sector,” *Phys. Rev. D* **90** (2014) 106004 [arXiv:1411.0798].

- [23] L. Nakonieczny, M. Rogatko and K. I. Wysokiński, “Magnetic field in holographic superconductors with dark matter sector,” *Phys. Rev. D* **91** (2015) 046007 [arXiv:1501.04902].
- [24] L. Nakonieczny, M. Rogatko and K. I. Wysokiński, “Analytic investigation of holographic phase transitions influenced by dark matter sector,” *Phys. Rev. D* **92** (2015) 066008 [arXiv:1509.01769].
- [25] M. Rogatko and K. I. Wysokiński, “P-wave holographic superconductor/insulator phase transitions affected by dark matter sector,” *JHEP* **03** (2016) 215 [arXiv:1508.02869].
- [26] M. Rogatko and K. I. Wysokiński, “Holographic vortices in the presence of dark matter sector,” *JHEP* **12** (2015) 041 [arXiv:1510.06137].
- [27] M. Rogatko and K. I. Wysokiński, “Condensate flow in holographic models in the presence of dark matter,” *JHEP* **10** (2016) 152 [arXiv:1608.00343].
- [28] Y. Peng, “Holographic entanglement entropy in superconductor phase transition with dark matter sector,” *Phys. Lett. B* **750** (2015) 420 [arXiv:1507.07399].
- [29] Y. Peng, Q. Pan and Y. Liu, “A general holographic insulator/superconductor model with dark matter sector away from the probe limit,” *Nucl. Phys. B* **915** (2017) 69 [arXiv:1512.08950].
- [30] C. Park, G. Kim, J. s. Chae and J. H. Oh, *JHEP* **02**, 182 (2023) doi:10.1007/JHEP02(2023)182 [arXiv:2210.08919 [hep-th]].
- [31] B. Kiczek, M. Rogatko and K. I. Wysokiński, “Holographic DC SQUID in the presence of dark matter,” arXiv:1904.00653.
- [32] M. Rogatko and K. I. Wysokiński, “Two interacting current model of holographic Dirac fluid in graphene,” *Phys. Rev. D* **97** (2018) 024053 [arXiv:1708.08051].
- [33] M. Rogatko and K. I. Wysokiński, “Holographic calculation of magneto-transport coefficients in Dirac semimetals,” *JHEP* **01** (2018) 078 [arXiv:1710.05002].
- [34] M. Rogatko and K. I. Wysokiński, “Viscosity bound for anisotropic superfluids with dark matter sector,” *Phys. Rev. D* **96** (2017) 026015 [arXiv:1612.02593].
- [35] X. Dong, S. Harrison, S. Kachru, G. Torroba and H. Wang, “Aspects of holography for theories with hyperscaling violation,” *JHEP* **06** (2012) 041 [arXiv:1201.1905].
- [36] B. Goutéraux and E. Kiritsis, “Generalized holographic quantum criticality at finite density,” *JHEP* **12** (2011) 036 [arXiv:1107.2116].
- [37] L. Huijse, S. Sachdev and B. Swingle, “Hidden Fermi surfaces in compressible states of gauge-gravity duality,” *Phys. Rev. B* **85** (2012) 035121 [arXiv:1112.0573].
- [38] M. Alishahiha, E. O. Colgain and H. Yavartanoo, “Charged Black Branes with Hyperscaling Violating Factor,” *JHEP* **11** (2012) 137 [arXiv:1209.3946].

- [39] G. Kim, Y. S. Choi and J. H. Oh, “Analytic approaches to anisotropic holographic superfluids in asymptotically hyperscaling violation geometry,” arXiv:2504.13635.
- [40] H.-S. Jeong, W.-B. Pan, Y.-W. Sun and Y.-T. Wang, “Holographic study of  $T\bar{T}$  like deformed HV QFTs: holographic entanglement entropy,” JHEP **02** (2023) 018 [arXiv:2211.00518].
- [41] G. Cavini, D. Seminara, J. Sisti and E. Tonni, “On shape dependence of holographic entanglement entropy in  $\text{AdS}_4/\text{CFT}_3$  with Lifshitz scaling and hyperscaling violation,” JHEP **02** (2020) 172 [arXiv:1907.10030].
- [42] C. Ran, S.-F. Wu and Z.-Y. Xian, “Learning geometries beyond asymptotic AdS,” JHEP **03** (2026) 031 [arXiv:2508.05808].
- [43] S. Ryu and T. Takayanagi, “Holographic derivation of entanglement entropy from AdS/CFT,” Phys. Rev. Lett. **96** (2006) 181602 [hep-th/0603001].
- [44] S. Ryu and T. Takayanagi, “Aspects of holographic entanglement entropy,” JHEP **08** (2006) 045 [hep-th/0605073].
- [45] S. N. Solodukhin, “Entanglement entropy, conformal invariance and extrinsic geometry,” Phys. Lett. B **665** (2008) 305 [arXiv:0802.3117].
- [46] L.-Y. Hung, R. C. Myers and M. Smolkin, “On holographic entanglement entropy and higher curvature gravity,” JHEP **04** (2011) 025 [arXiv:1101.5813].
- [47] H. Casini, M. Huerta and R. C. Myers, “Towards a derivation of holographic entanglement entropy,” JHEP **05** (2011) 036 [arXiv:1102.0440].
- [48] J. Bhattacharya, M. Nozaki, T. Takayanagi and T. Ugajin, “Thermodynamical property of entanglement entropy for excited states,” Phys. Rev. Lett. **110** (2013) 091602 [arXiv:1212.1164].
- [49] E. Bianchi and R. C. Myers, “On the architecture of spacetime geometry,” Class. Quant. Grav. **31** (2014) 214002 [arXiv:1212.5183].
- [50] M. Nozaki, T. Numasawa, A. Prudenziati and T. Takayanagi, “Dynamics of entanglement entropy from Einstein equation,” Phys. Rev. D **88** (2013) 026012 [arXiv:1304.7100].
- [51] V. Rosenhaus and M. Smolkin, “Entanglement entropy: a perturbative calculation,” JHEP **12** (2014) 179 [arXiv:1403.3733].
- [52] V. Rosenhaus and M. Smolkin, “Entanglement entropy, planar surfaces, and spectral functions,” JHEP **02** (2015) 015 [arXiv:1410.6530].
- [53] S. S. Gubser, “Colorful horizons with charge,” Phys. Rev. Lett. **101** (2008) 191601 [arXiv:0803.3483].
- [54] S. A. Hartnoll, C. P. Herzog and G. T. Horowitz, “Building a holographic superconductor,” Phys. Rev. Lett. **101** (2008) 031601 [arXiv:0803.3295].

- [55] S. A. Hartnoll, C. P. Herzog and G. T. Horowitz, “Holographic superconductors,” *JHEP* **12** (2008) 015 [arXiv:0810.1563].
- [56] C. P. Herzog, “Lectures on holographic superfluidity and superconductivity,” *J. Phys. A* **42** (2009) 343001 [arXiv:0904.1975].
- [57] G. T. Horowitz, “Introduction to holographic superconductors,” *Lect. Notes Phys.* **828** (2011) 313 [arXiv:1002.1722].
- [58] M. Park, J. Park and J. H. Oh, “Phase transition in anisotropic holographic superfluids with arbitrary  $z$  and  $\alpha$ ,” *Eur. Phys. J. C* **77** (2017) 810 [arXiv:1609.08241].
- [59] M. Ammon, J. Erdmenger, M. Kaminski and P. Kerner, “Superconductivity from gauge/gravity duality with flavor,” *Phys. Lett. B* **680** (2009) 516 [arXiv:0810.2316].
- [60] Z.-Y. Nie, R.-G. Cai, X. Gao and H. Zhang, “Competition between the s-wave and p-wave superconductivity phases in a holographic model,” *JHEP* **11** (2013) 087 [arXiv:1309.2204].
- [61] T. Nishida, “Phase diagram of a holographic superconductor model with s-wave and p-wave,” *JHEP* **09** (2014) 154 [arXiv:1403.6070].
- [62] W. Li, “Competition between s-wave order and p-wave order in holographic superconductors,” *JHEP* **11** (2014) 147 [arXiv:1405.0382].
- [63] R.-G. Cai, L. Li, L.-F. Li and R.-Q. Yang, “Introduction to holographic superconductor models,” *Sci. China Phys. Mech. Astron.* **58** (2015) 060401 [arXiv:1502.00437].
- [64] M. Ammon, J. Erdmenger, V. Grass, P. Kerner and A. O’Bannon, “On holographic p-wave superfluids with back-reaction,” *Phys. Lett. B* **686** (2010) 192 [arXiv:0912.3515].
- [65] J. Erdmenger, V. Grass, P. Kerner and T. H. Ngo, “Holographic superfluidity in imbalanced mixtures,” *JHEP* **08** (2011) 037 [arXiv:1103.4145].
- [66] S. A. Hartnoll, “Lectures on holographic methods for condensed matter physics,” *Class. Quant. Grav.* **26** (2009) 224002 [arXiv:0903.3246].
- [67] J. McGreevy, “Holographic duality with a view toward many-body physics,” *Adv. High Energy Phys.* **2010** (2010) 723105 [arXiv:0909.0518].
- [68] C. Charmousis, B. Gouteraux, B. S. Kim, E. Kiritsis and R. Meyer, “Effective holographic theories for low-temperature condensed matter systems,” *JHEP* **11** (2010) 151 [arXiv:1005.4690].
- [69] B. Gouteraux and E. Kiritsis, “Quantum critical lines in holographic phases with (un)broken symmetry,” *JHEP* **04** (2013) 053 [arXiv:1212.2625].
- [70] E. Kiritsis and J. Ren, “On holographic insulators and supersolids,” *JHEP* **09** (2015) 168 [arXiv:1503.03481].

- [71] S. Kachru, X. Liu and M. Mulligan, “Gravity duals of Lifshitz-like fixed points,” *Phys. Rev. D* **78** (2008) 106005 [arXiv:0808.1725].
- [72] M. Taylor, “Non-relativistic holography,” arXiv:0812.0530.
- [73] S. Bhattacharyya, S. Minwalla and K. Papadodimas, “Small hairy black holes in global AdS spacetime,” *JHEP* **11** (2011) 035 [arXiv:1005.1287].
- [74] P. Basu, J. He, A. Mukherjee and H.-H. Shieh, “Superconductivity from D3/D7: holographic pion superfluid,” *JHEP* **11** (2009) 070 [arXiv:0810.3970].
- [75] D. Mateos and D. Trancanelli, “The anisotropic N=4 super Yang–Mills plasma and its instabilities,” *Phys. Rev. Lett.* **107** (2011) 101601 [arXiv:1105.3472].
- [76] A. Rebhan and D. Steineder, “Violation of the holographic viscosity bound in a strongly coupled anisotropic plasma,” *Phys. Rev. Lett.* **108** (2012) 021601 [arXiv:1110.6825].